https://doi.org/10.5194/egusphere-2026-2045
Preprint. Discussion started: 21 April 2026

Fidelity and stratigraphy of the Antarctic Allan Hills old ice archive from Continuous Flow Analysis

Abigail Hudak[1], Asmita Banerjee[1], Christo Buizert[1], Edward Brook[1], Michael Kalk[1], Lindsey Davidge[2], Andrew J. Schauer[2], Eric J. Steig[2], Noah Brown[2], Liam Kirkpatrick[2], John-Morgan Manos[2], Jacob I. Chalif[3], Erich Osterberg[3], Miranda Miranda[4], Eric Saltzman[4], Yuzhen Yan[5], Valens Hishamunda[6], and John Higgins[6].

[1]College of Earth, Ocean and Atmospheric Sciences, Oregon State University, Corvallis, OR, 97331, USA

[2]Department of Earth and Space Sciences, University of Washington, Seattle, WA, 98195, USA

[3]Department of Earth and Planetary Sciences, Dartmouth College, Hanover, New Hampshire, 03755, USA

[4]Department of Earth System Science, University of California-Irvine, Irvine, CA, 92697, USA

[5]State Key Laboratory of Marine Geology, Tongji University, Shanghai, 200092, China

[6]Department of Geosciences, Princeton University, Princeton, NJ, 08544, USA

Correspondence to: Abigail Hudak (hudakab@oregonstate.edu)

Abstract. The Allan Hills blue ice area, East Antarctica, offers a unique opportunity to extend the ice core record beyond 800 thousand years (kyr), with ice as old as 6 million years recently recovered. The ice in this area demonstrates several peculiarities—such as strong layer thinning and folding—that warrant an in-depth investigation of its stratigraphy and the fidelity of the climate record it contains. Here, we present a high-resolution Continuous Flow Analysis (CFA) of two shallow ice cores from the Allan Hills (ALHIC 2201 and ALHIC 2302), spanning the upper 69 m and 46 m, respectively.

Our CFA analysis includes methane, water stable isotopes, and particle concentrations, allowing us to characterize their variability and assess how well geochemical measurements are recorded and preserved in Allan Hills ice. Dating of the ice (using the ^{40}Ar chronometer) revealed ages ranging from ~150–1200 kyr with substantial age discontinuities and folding, highlighting the complex stratigraphy of ice in this region. To assess glacial-interglacial variability, we conduct descriptive statistical analyses of each measurement relative to the EPICA Dome C (EDC) deep ice core record, which served as a reference benchmark over the last 800 kyr. Relative to EDC, we find data representing warm climate states are overrepresented at Allan Hills, and the Allan Hills records typically exhibit a narrower distribution compared to the EDC record. These observations confirm previous suggestions of interglacial bias and glacial cycle averaging in some sections of Allan Hills records. Differences between ALHIC 2201 and ALHIC 2302 further suggest that coring location within the Allan Hills region affects signal preservation in the record. Our high-resolution investigation of this ice is a critical step toward improved interpretation of the discrete, multi-million-year records from the Allan Hills.

https://doi.org/10.5194/egusphere-2026-2045
Preprint. Discussion started: 21 April 2026

1 Introduction

Marine and terrestrial sediment records have revealed major aspects of our Earth's climate history, extending millions of years into the past. Two significant climatic periods include the Mid-Pleistocene Transition (MPT; 0.8–1.2 Ma), where ice age pacing transitioned from a dominant 40 kyr to approximately 100 kyr periodicity (Berends et al., 2021; Clark et al., 2006; Ford & Chalk, 2020), and the mid-Pliocene Warm Period (mPWP; 3–3.3 Ma)—when surface temperatures were 2 to 5°C higher than pre-industrial which is sometimes suggested as analogue for future warming (Burton et al., 2025; Haywood et al., 2020; Tierney et al., 2025). While ice cores uniquely preserve past atmospheric composition, the longest continuous record available—EPICA Dome C (EDC)—extends only to ~800-kyr (EPICA community members, 2004) limiting our understanding of the coupling between atmospheric composition and climate further back in time. Extending the ice core record to older, climatically significant periods, such as the MPT, is a major goal of the ice coring community with potential to address outstanding questions regarding the mechanistic underpinnings and feedbacks of the climate system (Paul Voosen, 2021; Severinghaus et al., 2010).

Blue ice areas (BIAs) provide a valuable opportunity to extend the ice core archive beyond the current 800-kyr continuous record (J. A. Higgins et al., 2015; Spaulding et al., 2012). The Allan Hills BIA in East Antarctica is of particular interest as 6-million-year-old ice has been recovered there at relatively shallow depths (~200 m) (Shackleton et al., 2025). Although the mechanisms of old ice preservation are not fully understood, the slow surface flow velocities, net ablation, and the uplift and stagnation of deep, older ice layers flowing into the Transantarctic Mountains likely facilitate the preservation of ancient ice at the Allan Hills (Bintanja, 1999). Unlike traditional deep ice cores recovered from the ice sheet interior, these records are subject to complex ice flow regimes, resulting in substantial ice layer thinning, folding, and discontinuities (Shackleton et al., 2025)

These discontinuous records provide valuable "snapshots" of past environmental conditions beyond the continuous record (Higgins et al., 2015; Marks-Peterson et al., 2026; Shackleton et al., 2025, 2026; Yan et al., 2019). These snapshots have been described as "short snapshots", indicating that some glacial-interglacial variability is preserved, or " long snapshots", indicating that they average over one or more glacial-interglacial cycles and preserve only the long-term secular trends (Marks Peterson et al. in press). These two snapshot types are inferred from age density estimates (yr cm^{-1}) and discrete measurements of CO_2, CH_4, $\delta^{18}O_{atm}$, and $\delta^{18}O_{ice}$ from dated ice core samples from the Allan Hills (Shackleton 2025, Shackleton 2026, Marks Peterson, et al., 2026).

https://doi.org/10.5194/egusphere-2026-2045
Preprint. Discussion started: 21 April 2026

Notably, the short snapshots appear to have an overrepresentation of interglacial values (i.e., the values are near interglacial maxima) and generally lack glacial values. In contrast, the long snapshots appear to reflect a glacial-interglacial average, although the relative contributions of interglacial and glacial ice to the average are yet to be fully. Determining the extent of possible biases in the Allan Hills archive, and how they may influence the preservation of climatically important periods such as the MPT and mPWP, is essential for interpreting ancient ice from this site.

Continuous flow analysis (CFA) can provide high-resolution (cm-scale) measurements of multiple geochemical measurements on the same section of ice and has been instrumental in revealing high-resolution details within ice core records (Jones et al., 2017a; Lambert et al., 2012; Osterberg et al., 2006; Rhodes et al., 2015). A new multi-measurement CFA system was developed as part of the National Science Foundation Center for Oldest Ice Exploration (NSF-COLDEX) to measure methane, particle concentrations, and water stable isotope ratios ($\delta^{18}O$ and $\delta^{2}H$) in Allan Hills cores. Here, we present CFA analyses for two cores, ALHIC 2201 and ALHIC 2302 in conjunction with atmospheric ^{40}Ar age dating of discrete samples (Bender et al., 2008; Shackleton et al., 2025) to evaluate stratigraphy and the fidelity of the Allan Hills archive.

To better understand the climate record and signal preservation at the Allan Hills, we aim to characterize each geochemical measurement (methane, dust, and water isotopes) in ALHIC 2201 and ALHIC 2302. We compare these data with the EDC record, which we use as a benchmark for glacial-interglacial variability. Examining the distributional characteristics of each measurement (e.g., variances, means, extrema, etc.) and comparing them to EDC serves as a first-order assessment of preservation of signals in the Allan Hills cores. To assess potential interglacial bias and signal smoothing, we compare how climate states are proportionally represented in the Allan Hills versus EDC. Together, these analyses are an important step toward better interpreting these novel Allan Hills records that extend the ice core record further back in time.

2 Methods

2.1 Study site and samples

Several decades of research in the Allan Hills in southern Victoria Land, Antarctica has led to the discovery of ancient meteorites up to 2.2 million years old on the surface of the ice (Scherer et al., 1997; Whillans & Cassidy, 1983), sparking interest in ice core drilling campaigns to recover old ice for paleoclimate reconstructions (Higgins et al., 2015) (Fig. 1). The glaciological setting at the Allan Hills (steep bedrock topography and nunataks, slow horizontal flow, and net ablation) leads to exhumation of old ice at the surface and contributes to the preservation of even older ice at depth near the bed (Grinsted et al., 2003). The lateral ice flow velocity through the main ice field (MIF) is approximately 60 cm $a^{-1,}$ decreasing to nearly 0 cm a^{-1} at an outcropping nunatak where the ablation rate is ~4.6 cm a^{-1} (Spaulding et al., 2012).

The two ice cores used in this study, ALHIC 2201 and ALHIC 2302 (Fig. 1), were drilled with the 24-cm diameter Blue Ice Drill (BID) (Kuhl et al., 2014) during the 2022-2023 and 2023-2024/2024-2025 field seasons, respectively. The two core drilling sites are located ~1.5 km apart but likely represent two distinct flow regimes: ALHIC 2201 (76.732 °S, 159.360 °E) is located proximally to the primary ice flow path while ALHIC 2302 (76.745 °S, 159.375 °E) is closer to a nunatak (Fig. 1). ALHIC 2201 is drilled in the vicinity of ALHIC 1901 which contains 4 Ma basal ice, while ALHIC 2302 was drilled nearby the site of ALHIC 1902 which contains basal ice dating to 6 Ma (Shackleton et al., 2025).

CFA analyses were conducted only on continuous, high-quality sections of the upper approximately 69 m of ALHIC 2201 and 46 m of ALHIC 2302; below these depths, core-quality deterioration precluded CFA analysis, although the cores extend to bedrock at ~90 m and ~186 m, respectively. While the origin of the unusual brittleness of the Allan Hills ice is not completely understood, it is likely related to the high-strain regime experienced by the ice as evidenced by elongated bubbles (Fitzpatrick et al., 2014). The proximity of ALHIC 2302 to the nunatak may be the cause of a higher concentration of rocks and particles found throughout the core that may have also contributed to lower-quality ice drilled at depth with the BID.

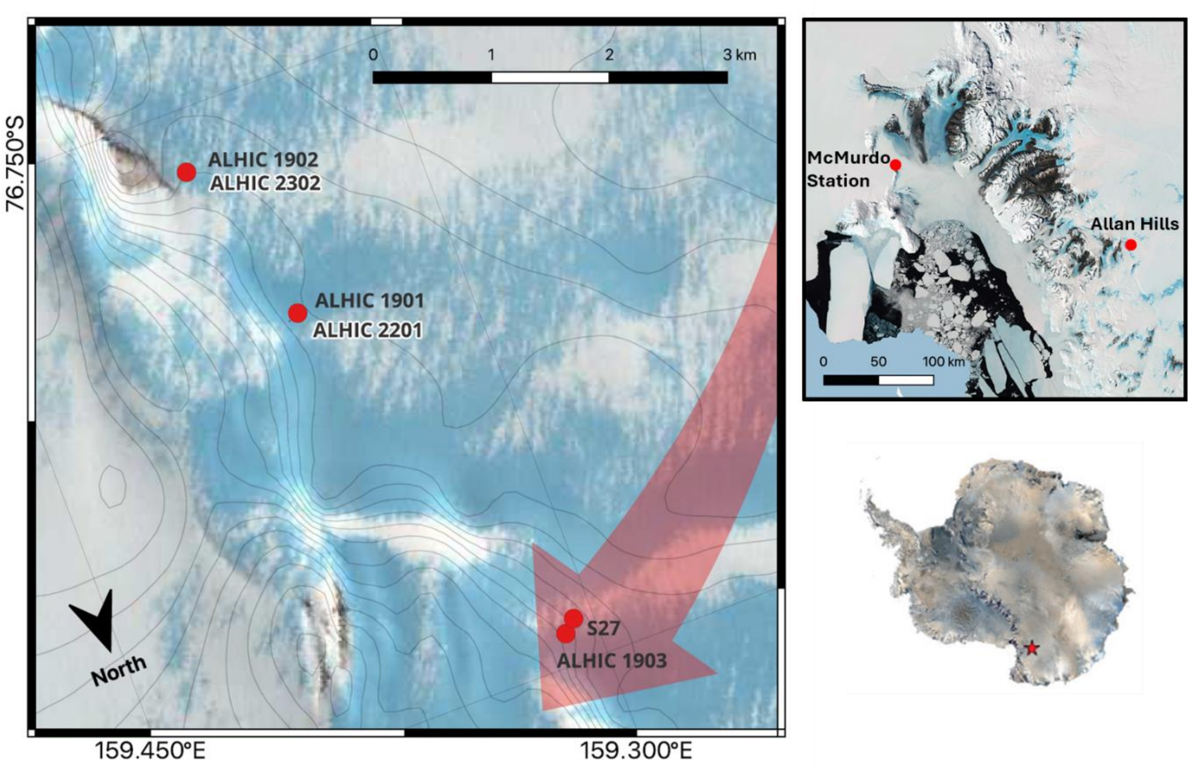

Figure 1. Map of the Allan Hills, Victoria Land, East Antarctica (left; Landsat Image Mosaic of Antarctica Project). The two cores analysed in this study—ALHIC 2302, located near a nunatak, and ALHIC 2201, located closer to the main ice field (MIF) flow line (red arrow)—are labeled and highlighted. Red circles indicate sites analysed, discussed, or referenced herein. The lower right map

shows the approximate location of the Allan Hills in Antarctica, marked by a red star. The upper right map shows the location of the Allan Hills relative to McMurdo Station (red dots).

2.2 Continuous flow analysis system

2.2.1 Analytical system

An updated version of the Oregon State University (OSU) CFA system, originally designed to analyze atmospheric gases (CH_4 and CO) (Rhodes et al., 2015), was extended to include the University of Washington's water stable isotope ($\delta^{18}O$, $\delta^{17}O$, and δ^2H) CFA system (which is based on earlier work of Davidge et al., 2022; Gkinis et al., 2011; and Jones et al., 2017), and a laser particle sensor (Abakus ®) to measure dust counts for particles between sizes of 0.8 to 10 µm.

The melter head system is installed in a -25 °C freezer, and designed to melt ice core sticks with a 3.5 x 3.5 cm cross section, of which, meltwater from only the inner 2.7 x 2.7 cm cross-section are used for analyses, while the outer portions are pumped to waste, preventing contamination from the outer surface in analyses (this is primarily an issue for dust and gas measurements). The melthead temperature is kept at ~15-18°C to maintain a constant melt rate of ~3.0 cm min-1 (Fig. 2A). Peristaltic pumps transfer the meltwater towards a custom-made debubbler that physically separates the entrapped air bubbles (~10% of the sample volume) and water.

As air from the debubbler moves towards the methane analyzer (Fig. 2B), a diaphragm pump downstream of the analyzer creates a pressure gradient that allows gas to be extracted from the water-gas mixture by a gas-permeable membrane module (Liqui-Cel, G591). The air sample is then dehumidified before entering the analyzer using a Nafion^{TM} drier with a backflow of dry N_2 gas. Measurements of CH_4 were made with a cavity-ring down spectrometer (CRDS, Picarro G2401), modified to have a small effective cavity volume by operating at reduced cavity pressures (40 torr) (Rhodes et al., 2015). The CRDS also measures CO (not reported here) and CO_2 (which is impacted by dissolution into the meltwater and also not reported) as well as water vapor.

Meltwater flow from the debubbler is split, with one flow transferred towards the water isotope system (Fig. 2C), where it enters a vaporization oven, held at 170 °C, comprised of a post-column reaction tee (part number TCEF411T, VICI, Houston, TX, USA) which functions in place of the glass nebulizer used in Jones et al. (2017), and a 16 mm ID x 45 cm long quartz tube that is open to the atmosphere. A 1/16" OD stainless steel tube, held at 90 °C, draws the vaporized sample from the inside of the glass tube and conveys the sample to the inlet of the CRDS water isotope analyzer. A Picarro L2140-i was used for ALHIC 2201 and a Picarro L2130-i was used for ALHIC 2302. The L2140-i was designed to include $\delta^{17}O$ (not considered here) but is otherwise functionally identical to the L2130-i (Schauer et al., 2016; Steig et al., 2014). Isotopic values for $\delta^{18}O$ and δ^2H are calculated as the deviation of heavy to light isotopic ratios in the sample (R_{sample}) from the Vienna Standard Mean Ocean Water (VSMOW) international standard $\delta = \frac{R_{Sample}}{R_{VSMOW}} - 1$, and normalized to the VSMOW-SLAP scale (Schoenemann et al., 2013), where SLAP is Standard Light Antarctic Precipitation ($\delta^2H = -428$‰, $\delta^{18}O = -55.5$‰), and R is the ratio of $^{18}O/^{16}O$ or $^2H/^1H$, respectively. Deuterium excess, *d*, is defined as the deviation from the linear meteoritic water line: $d = \delta^2H - 8 \times \delta^{18}O$. All δ values are reported in ‰ (per mille).

Meltwater in a second line of the split is peristaltically pumped to the laser particle sensor (Fig. 2D). Particles in the meltwater were counted and sized by a Klotz Abakus® instrument that measures the light attenuation as particles pass through, thereby quantifying the counts and size of particles in the meltwater. Size fractions were allocated to 32 size bins between 0.8 and 10 microns. Particle counts were converted to concentration (particles mL^{-1}) using data from a flow rate sensor (Sensirion EK-SLI-2000) directly upstream of the Abakus®. The water flow towards the laser particle detector is maintained at approximately 4 mL minute^{-1}. We report dust concentrations using number concentrations (particles mL^{-}1) rather than mass concentration (e.g., μg L-1), due to the density and spherical shape assumptions required to convert laser particle measurements to mass (Chesler et al., 2022; Simonsen et al., 2018). Interpreting dust size fractions from an Abakus® requires calibration with an instrument that accurately measures particle volume (e.g., a Coulter Counter). Due to this limitation, along with a software issue during the ALHIC 2302 measurement campaign, we do not report dust size data here.

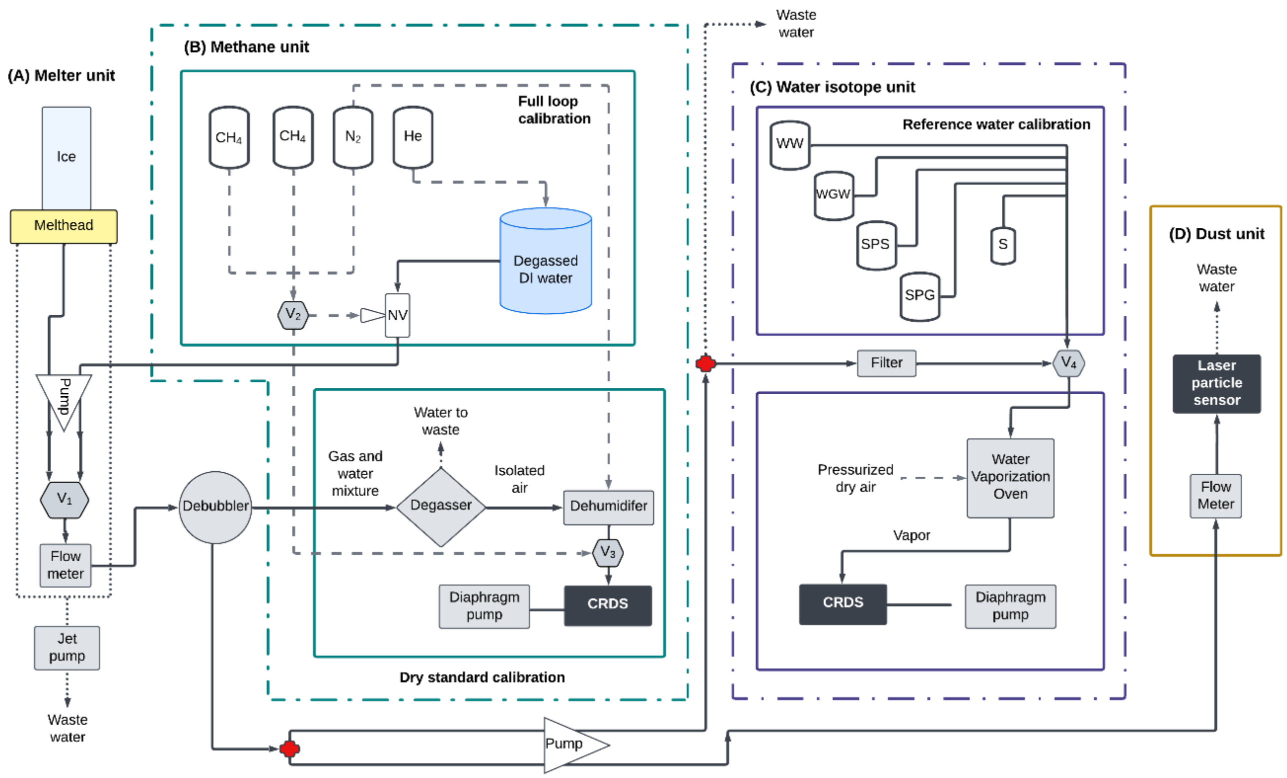

Figure 2. Configuration of the continuous flow analysis (CFA) system to analyze methane, water isotopes, and dust concentrations (see Section 2.2.1 for details). For the gas and water isotope units, upper boxes represent calibration systems and lower boxes represent the analyzing components, with the entire unit outlined in a dash-dot line. Dotted lines indicate wastewater; dashed lines are dry gas pathways; solid lines show sample flows; and red crosses mark physical splits.

Sample analysis: Ice sticks are melted on a temperature-controlled melthead (A) inside a freezer room. Meltwater from the inner portion of the ice stick is peristaltically pumped towards the analyzer systems while the outer portions of the ice stick are transferred to waste via a jet pump. The mixture of gas and water is peristaltically pumped to a custom debubbler, passing a flow meter. The bubbles from the debubbler are transferred to the gas extraction unit (B) where the sample is further degassed by a gas-permeable membrane module and dehumidified using a custom-built Nafion dryer with backflowing N_2 gas, before entering the cavity ringdown spectrometer (CRDS). Water from the debubbler is pumped into the water isotope (C) and dust (D) units. In the water isotope unit, water is further degassed before entering a water vaporization oven to create vapor that enters a CRDS. Water entering the dust unit passes a flow meter and a laser particle sensor where the water is then exported to waste.

Calibration: Water entering the analyzers is selected via valve V1 between degassed deionized (DI) water and ice-core meltwater. The methane unit includes two calibration modes: a full loop wet standard, which combines degassed (via He bubbling) DI water with a CH_4 gas standard via a needle valve (NV) controlled by valve V_2; and a dry-standard calibration, which introduces dry CH_4 or N_2 gas directly into the CRDS via valve V_3. For the water isotope unit, four reference waters (labeled WW, WGW, SPS, SPG, and a standby, S) are entered into the analyzing stream via valve V_4 which also controls whether the water analysed is a reference water or the ice core sample.

2.2.2. Calibration

The solubility of CH_4 in water results in reduced concentrations in the CFA system (Rhodes et al., 2013; Stowasser et al., 2012). The solubility effect was corrected following methods of Rhodes et al. (2013) and Stowasser et al. (2012) by measuring the offset between the *full loop* (wet standard) calibration and the *dry standard* calibration at the beginning and end of each campaign day (Fig. 2B). The full loop calibration mixes standard air with water, with the mixture then going through the full gas extraction process. The air/water mixture is created by first degassing deionized water via stirring and helium bubbling and then adding a NOAA-calibrated CH_4-in-air standard to the degassed water at a 1:9 volumetric ratio (to resemble an ice core sample). Dry standard calibration refers to direct input of the dry NOAA-calibrated CH_4-in-air standards (scale: NOAA2004 scale; reference gases: CA04382 384.89 ± 0.06 ppb and CA04332 667.30 ± 0.21 ppb) into the CRDS.

To validate the calibration routine, discrete samples were measured for CH_4 at OSU from an adjacent piece of ice. Methods for discrete CH_4 analysis at OSU are described in Epifanio et al. (2020). After excluding the upper 10 m of the core to avoid the effects of surface cracking and modern air contamination, the discrete CH_4 measurements show a mean offset of −0.29 ppb ± 53.2 ppb (1σ) relative to the CFA record at the same depth intervals of the discrete samples. The large standard deviation arises from several mismatches between the datasets that may arise due to depth misaligns in post-processing, stratigraphic offsets, undetected lab air intrusions, or biological alterations. The overall small offset between the discrete and CFA data validates our solubility correction.

The water isotope data were calibrated using reference water measurements at the beginning and end of each campaign day (Fig. 2C). The four reference waters covering a spread of Antarctic values were previously calibrated directly to the VSMOW-SLAP scale (Schauer et al., 2016; Schoenemann et al., 2013; Steig et al., 2014). The δ^2H and $\delta^{18}O$ (‰) values for the reference waters are as follows: WAIS Water (WW; δ^2H = –268.30, δ^{18}O = –33.82), WAIS Glacial Water (WGW; δ^2H = –318.82, δ^{18}O = –39.77), South Pole Snow (SPS; δ^2H = –365.01, δ^{18}O = –46.96), and South Pole Glacial (SPG; δ^2H = –435.31, δ^{18}O = –55.39). The reference waters were sequentially pumped through the water isotope system and used to calibrate the measured sample values using a three-point linear regression, thereby normalizing CFA measurements to the VSMOW-SLAP scale. Daily calibrations were not significantly different from the entire campaign average, and therefore, an average global slope and intercept were used.

Discrete samples were also analysed at the University of Washington from the drilling chips collected from each coring drill run. These measurements agree well with our CFA water isotope measurements, confirming our calibrations (Fig. 3). Offsets between discrete and CFA measurements (mean ± 1σ of bias-corrected differences) were 0.005 ‰ ± 0.34 ‰, 0.39 ‰ ± 2.34 ‰, and 0.39 ‰ ± 2.34‰ for δ^{18}O, δ^2H, and *d* in ALHIC 2201, and 0.36 ‰ ± 0.37 ‰, –0.31 ‰ ± 3.26 ‰, and –3.20 ‰ ± 1.18 ‰ in ALHIC 2302, respectively.

We did not calibrate dust measurements, but Abakus concentrations on ALHIC 2302 were replicated during a CFA campaign at Dartmouth College (DC), providing a useful inter-lab comparison. Dust concentration data from the OSU and DC campaigns exhibit highly similar variability and are strongly correlated on a 10-cm scale (spearman rank correlation = 0.72), indicating that both systems captured the same signal (Fig. A1). Methods for the DC CFA system are described in Osterberg et al. (2006) and Winski et al. (2019). For water isotopes, dust, and CH_4, ALHIC 2201 depths 55.8 to 69 m were replicated on an adjacent CFA stick to evaluate reproducibility of our analytical systems (Fig. A2).

2.2.3. Campaign procedures

Samples for CFA were cut into 3.5 x 3.5 cm ice sticks with lengths varying from 6 to 100 cm, depending on the core quality. Some ALHIC 2201 sticks cracked in transit, exacerbating problems related to poor core quality in drilling. Before each CFA stick was placed on the melter, the ends were scraped with a Milli-Q® -rinsed metal scalpel to remove any lab-introduced particles. Each day of the campaign, analysis began and ended with water isotope and CH_4 calibration. Ultra-pure Milli-Q® water was frozen in layflats and cut to mimic ice core sticks. Before the start of analysis each day, Milli-Q® ice was first melted using the melter system to flush the lines and remove any impurities. Before and after a series of ALHIC samples were measured, sticks of Milli-Q® along with Taylor Glacier ice that was analysed in Baggenstos et al. (2018) with known glacial and interglacial sections were placed on the melter to confirm analytical systems were functioning properly, designate a clear start and end to ALHIC data, and to calculate response times. The time each new ice stick reached the melter was recorded, as was the time the top of the stick passed 10 cm interval markings. This information was used to calculate the melt rate and to align data from the analysers to each ice stick to create a depth log.

2.2.4. Data processing, depth translation, and sample resolution

Each core section had an assigned top and bottom field depth from collection at the field site. Each stick was trimmed to have flat, perpendicular top and bottom surfaces for melting. The length removed from the top and bottom of the stick were recorded and used to refine the true top and bottom depths from the field-assigned depths. To assign depths to the data, the times of the core section reached the melthead plus an offset for the travel time to each analyser were matched to the data (assuming a constant travel time that was pre-determined).

The effective measurement resolution varies between the gas, water isotope, and dust measurements. Response times were estimated experimentally by placing sticks with different concentrations on top of each other and observing how long the measured transition took to progress from 10% to 90% of the concentration difference (Fig. A3, Stowasser et al., 2012). The effective spatial resolution was calculated as the product of the response time and the average melt rate (3 cm min^{-1}). The response time and spatial resolution for CH_4 were estimated to be 128 s and 6.4 cm, respectively, evaluated via alternating 20 cm sections of Taylor Glacier glacial and interglacial ice (Baggenstos et al., 2018). For water isotope and dust response time and spatial resolution calculations, Milli-Q ice sticks were alternated with Taylor Glacier ice. The response time and spatial resolution for $\delta^{18}O$ were 44 s and 2.2 cm, and for dust were 5 s and 0.25 cm, respectively. For consistency and convenience, a 5-cm binning was applied across all datasets for analyses presented here. We validated that performing the analyses at the effective resolution of each data type (e.g., average depth bin of 0.25 cm for dust) gives identical results.

Contaminated data (e.g., lab air intrusions that impact gas measurements and post-debubbler air bubbles that impact dust and water isotope measurements) were evaluated for each dataset (CH_4, dust, and water isotopes). Lab air intrusions are problematic for CH_4 measurements in that they create large spikes in the data (modern atmospheric air is >250% of the CH_4 ice core record average). These intrusions usually resulted in a notable change in instrumental measurements of the CH_4 CRDS, such as a spike in the cavity pressure. Spikes in the CH_4 data and cavity pressure were used to diagnose data to be removed.

Additionally, large spikes in CH_4 were removed from the dataset even if they did not have a change in cavity pressure, if they occurred after a core break (transition to a new stick) and there was no simultaneous change in water isotopes or dust (suggesting that the feature was not a climate signal). Surface cracking in the upper 10 m of the glacier can result in elevated methane values due to the intrusion of modern air; the top 10 m of CH_4 data was removed from the analyses presented here. Residual air bubbles formed after degassing caused noticeable artifacts in the water isotope and dust data and were accompanied by flow rates of 0 ml min^{-1}; these data were subsequently removed.

2.3 Dating

Samples selected for dating were chosen both at regular intervals along the core and at locations where abrupt geochemical measurement variations showed suspected stratigraphic discontinuities (e.g., folding) or abrupt climatic transitions. Dating of the ice utilized the ^{40}Ar geochronometer, which estimates age from the gradual accumulation of ^{40}Ar in the atmosphere that reflects the decay of ^{40}K to ^{40}Ar in the solid Earth and outgassing of ^{40}Ar into the atmosphere (Bender et al., 2008). The age is derived from the deficit of ^{40}Ar in ancient air trapped in ice relative to the modern atmosphere. The absolute age uncertainty is ±11% (1σ) for ice older than 600 kyr. For ice younger than 600 kyr, the instrumental precision (± ~60 kyr, 1σ) is considered as it exceeds the absolute uncertainty estimate (Shackleton et al., 2025). When comparing relative age differences between samples, the instrumental precision (~60 kyr) provides the most relevant uncertainty estimate. The samples used for dating were from an adjacent piece of ice and covered approximately 15 cm in depth.

2.4 EDC datasets

The EPICA Dome C (EDC) datasets for water isotopes (Landais et al., 2021), dust (Lambert et al., 2008), and methane (Loulergue et al., 2008) were used as a comparison benchmark to the ALHIC datasets described in this study. Notably, the Abakus instrument used at the University of Bern for EDC dust measurements measured different size bins than OSU, ranging from 1 to 17.2 µm (versus 0.8 to 10 µm) which may influence differences observed between the datasets. All EDC records used in this study only include ages > 200 years to omit any substantial anthropogenic climate signals. EDC data were analysed by depth (as opposed to age) unless otherwise stated.

3. Results and Discussion

Our CFA records of dust, water isotopes ($\delta^{18}O$ and $\delta^{2}H$), and CH_4 on the upper layers of ALHIC 2201 and 2302 reveal new insights on the paleoclimate archive at the Allan Hills (Fig. 3). All the geochemical measurements covary in predictable ways (i.e., warmer climate states have higher CH_4 and water isotope values, and lower dust concentrations). The similarity in the covariation patterns to EDC (Fig. 4, Table A1) supports the reliability of our CFA measurements and confirms that Allan Hills, despite its complexities, preserves relationships between environmental signals. The following sections examine the implications of the observed data distributions for understanding stratigraphic complexities, variance, bias, and the effects of accumulation and thinning across the geochemical measurements of the ALHIC records.

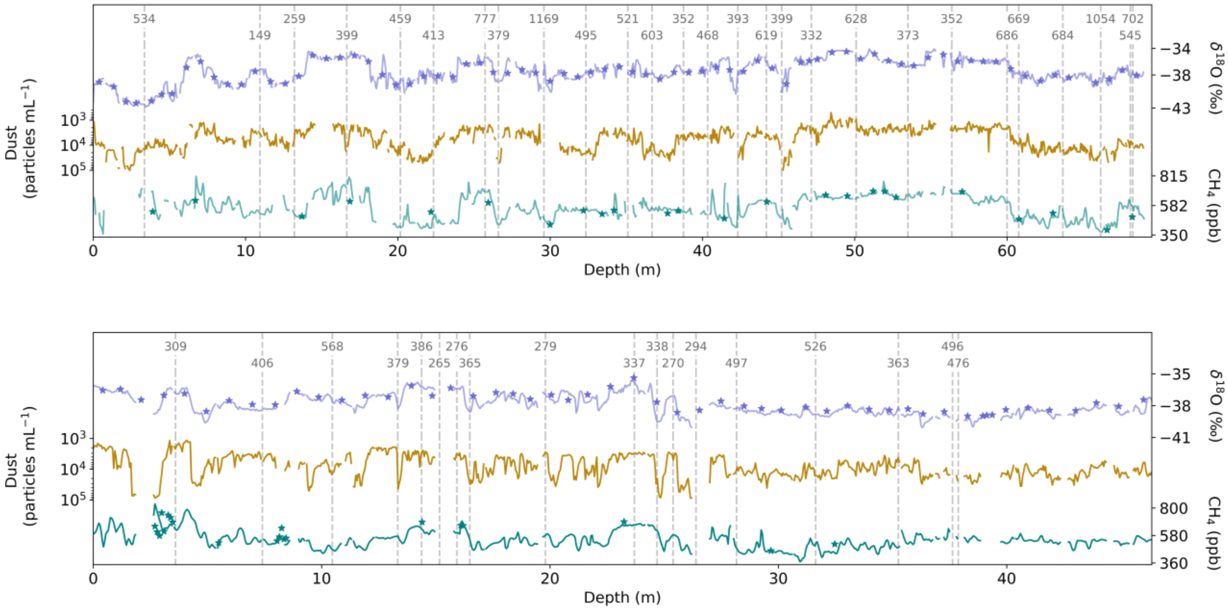

Figure 3. Continuous Flow Analysis (CFA) data for the upper 69.0 m of ALHIC 2201 (top) and for the upper 46.4 m of ALHIC 2302 (bottom). Data are averaged on a 5 cm depth scale for $\delta^{18}O$ (per mil; top, purple), log-transformed dust concentrations (particles mL^{-1}; middle, goldenrod), and CH_4 (ppb; bottom, teal). Discrete $\delta^{18}O$ from drill chips are represented by stars on top of the $\delta^{18}O$ CFA data and discrete CH_4 from an adjacent CFA stick are represented as stars on top of the CH_4 CFA. Vertical dashed grey lines and their corresponding numbers represent the ^{40}Ar age in kyr BP at the mean depth of the ^{40}Ar samples. Gaps in the record are due depths not analysed because of removed ice sections (due to poor core quality) or due to post processing removal of data due to contaminated or altered data.

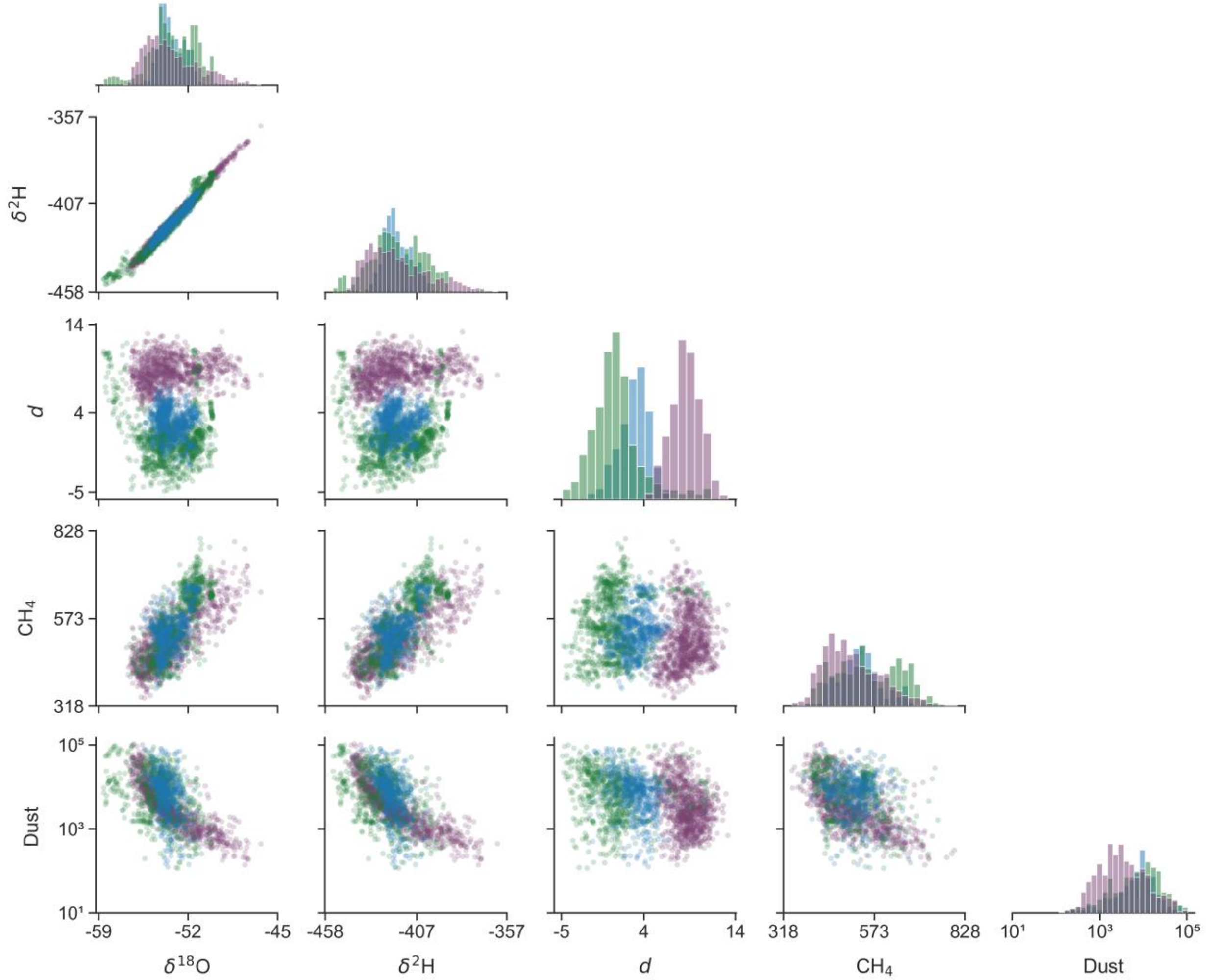

Figure 4. Pairwise relationships among $\delta^{18}O$, δ^2H, *d*, CH_4, and dust concentrations for ALHIC 2201 (green), ALHIC 2302 (blue), and EDC (purple). The EDC dataset was binned at a 1 m scale and was randomly sampled to n = 1000 to account for the differences in sample sizes between the EDC and ALHIC datasets. The off-diagonal panels display scatter plots for each variable pairing, and diagonal panels show histograms based on pairwise data. (Note that these pairwise data histograms will show different distributions than the Kernel Density Estimations in Fig. 6 as these pairwise data are based on the subset of depth bins where both variables in a given pair are available.) Corresponding regression and correlation statistics are summarized in Table A1.

3.1 Stratigraphy

The ^{40}Ar dates show substantial age discontinuities throughout both the ALHIC 2201 and 2302 cores (Fig. 5A). While most of the ages in the upper layers overlap with the 800 kyr continuous ice core record, two samples in ALHIC 2201 exceeded 1 Ma. The wider age range of ALHIC 2201 (~150–1170 kyr) compared to ALHIC 2302 (~264–568 kyr) may reflect their different positions within the ice field, where local ice flow dynamics may influence age distribution and stratigraphic layer preservation (Fig. 1). Uneven ^{40}Ar dating sample spacing along the depth of the core may have introduced a small bias in the age distributions observed (Fig. 3).

Evidence of meter-scale folding is apparent in ALHIC 2201 between ~42 and 45 m, where two similar ages occur at ~42 and 45 m (393 and 399 kyr, respectively), surrounding a dissimilar age at 44 m (619 kyr) (Fig. 5B). All three climate proxies covary and show a mirrored sequence, indicating a potential fold. (Kirkpatrick et al., 2025) finds that layer dip angles in the upper layers of ALHIC2201 are consistent over depth. This result is supported by visible, near-parallel englacial layers in radar data near this site (Nesbitt and Brook, 2023). Kirkpatrick et al. suggested that the apparent contradiction between parallel layering and stratigraphically disturbed age scales may be explained by recumbent folds. In this scenario, folding would occur in place or upstream and be drawn into parallel layers by ice flow and thinning.

When comparing dated CFA sections to the EDC record, the Allan Hills data do not always align with the expected EDC values. While some offsets may arise from age uncertainties, large discrepancies may reflect mixing—where ice packets of different ages have been incorporated within the depth section from which the ^{40}Ar age was measured. For instance, if 800 kyr and 200 kyr ice were equally mixed, the resulting analytical age could appear as ~500 kyr, though the corresponding signal would not represent climate conditions at that time. Alternatively, some mismatches, particularly in the water isotope data, may be indicative of ice originating from a different source region. For example, the very low δ^{18}O values observed in ALHIC 2201 with an apparent age of ~534 kyr at ~3 m, along with high *d*, may indicate ice derived from the interior East Antarctic or at a higher elevation site rather than the local Allan Hills accumulation zone (Fig. A4). Conversely, dated records that do align well may indicate preserved, continuous sections of the climate record as indicated by alignment of δ^{18}O, *d*, CH_4, dust, and ^{40}Ar age at ~340 kyr, which may be indicative of Termination IV.

Stratigraphically intact ice cores have been recovered at the Allan Hills, such as ALHIC 1903 (76.7026 ° S, 159.31081 ° E) and S27 (76.70°S, 159.31°E), along the main ice flow line through the MIF (Fig. 1; Carter et al., in press.; Shackleton et al., 2025; Spaulding et al., 2012). The age discontinuities present in ALHIC 2201 and 2302, located just ~3.5 and 5 km away from the S27/1903 site, respectively, suggest that small deviations from the main flow line can result in stratigraphic disturbances. However, it must be noted that no cores have been drilled to bedrock along the main flowline, and therefore the extent of stratigraphic continuity at depth is unknown. Additionally, despite being separated by just ~1.5 km, ALHIC 2302 (closer to the nunatak) and ALHIC 2201 (closer to the MIF) exhibit substantially different age ranges in the CFA analysis depth range and throughout the entire core (see Section 3.4). These features highlight the influence of local topography, ice flow dynamics, and post-depositional processes on stratigraphic patterns in ALHIC ice cores.

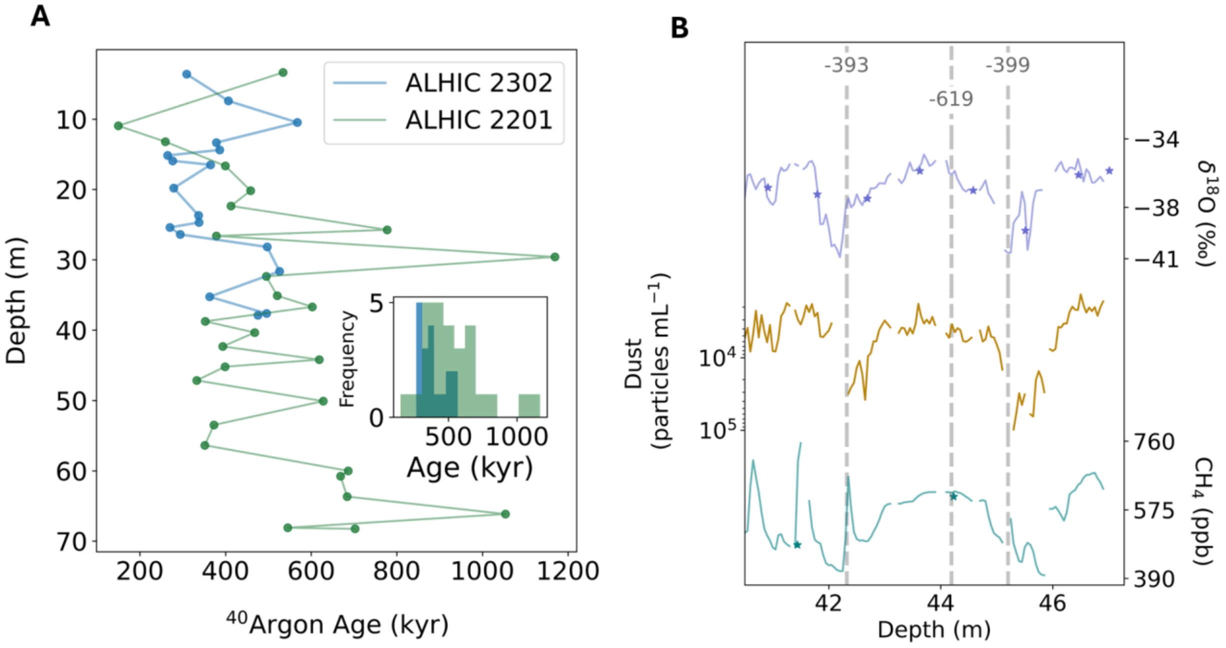

Figure 5. Age stratigraphy and an example of potential folding in ALHIC 2201. A: ^{40}Ar ages as a function of depth (m) for ALHIC 2201 (green) and ALHIC 2302 (blue) and as a distribution (inset). Age uncertainties are 60 kyr for ages < 600 kyr and 11 % of the age for ages > 600 kyr. B: Evidence for potential meter-scale folding in ALHIC 2201. These depths were deliberately sampled to identify whether the two peaks in the three datasets were similar ages with a different age in between. Data are averaged on a 5 cm depth scale for δ^{18}O (‰; top, purple), log-transformed dust concentrations (particles mL^{-1}; middle, goldenrod), and CH_4 (ppb; bottom, teal). All data is as in Fig. 3.

3.2 Proxy distributions: signal variance and attenuation

Understanding signal variance and attenuation in Allan Hills ice is of particular interest due to their implications for interpreting the oldest ice, as evidenced by the inferred short and long snapshots discussed previously. Several post-depositional processes may contribute to signal attenuation in the Allan Hills ice. As ice flows away from the accumulation site and slows, folding, shearing, physical mixing, recrystallization, and layer thinning may complicate the preservation of environmental signals. Complex ice flow, variable rheology, and steep bedrock topography surrounding the nunatak likely further enhance folding and complicate the stratigraphy.

The range of preserved values within the geochemical measurements suggests that some glacial-interglacial variability is preserved, but there appears to be a bias towards interglacial values. All geochemical measurements, except for ALHIC 2201 CH_4, have less variance than EDC, with the strongest reductions seen in ALHIC 2302 (Table 1). To further examine modifications of the signals, we first discuss the degree of attenuation in ALHIC 2201 and 2302 by comparing the distributions of each measurement with EDC (Fig. 6). These distributions provide insight into the attenuation: the width reflects the extent of glacial–interglacial variability preserved, while the overall shape indicates which climate states are over- or underrepresented.

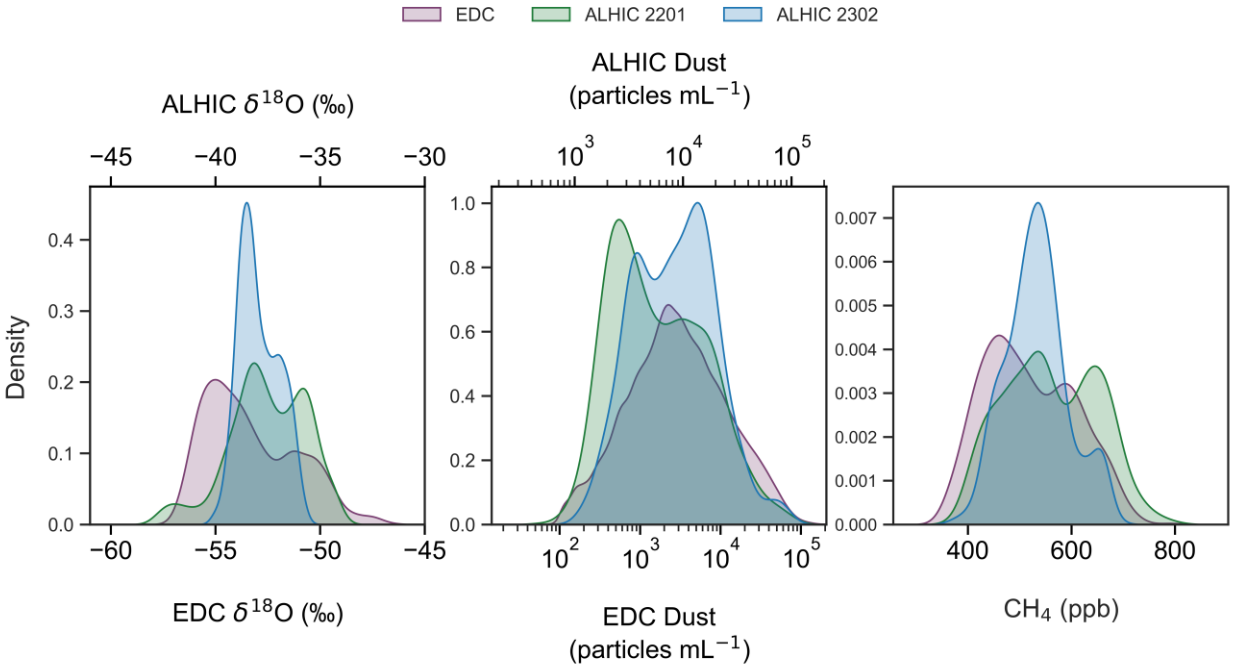

Figure 6. Kernel density estimations (KDEs) for $\delta^{18}O$ (‰, left), dust concentrations (particles mL^{-1}, middle), and CH_4 (ppb, right) for ALHIC 2201 (green), ALHIC2 2302 (blue), and EDC (purple). For $\delta^{18}O$ and dust the means were aligned as there is an expected mean offset due to regional climatic and depositional differences, and possible small instrumentation offsets, so these are plotted with separate x-axes with the ALHIC axis on top and EDC on the bottom.

Atmospheric methane is expected to be homogeneous across Antarctica as it is globally well-mixed in the atmosphere. The distributions of CH_4 for EDC and both ALHIC cores were bimodal, and for ALHIC 2302, variance was reduced relative to EDC (~75% of EDC; Table 1, Fig. 6). Methane values for ALHIC 2201 exhibited similar variance and range of values compared to EDC (range is approximately equal), but with substantially more data in the higher CH_4 range resulting in a broader high-value mode, as discussed further in Section 3.3.1. Elevated levels of CH_4 may arise due to CH_4 derived from undetected laboratory air intrusions, from biological alteration (i.e., methanogenesis) in situ in the ice, or produced due to high dust concentrations within the analytical line (Lee et al., 2020; Mühl et al., 2023).

Proximity to the nunatak likely influences the dust concentrations due to interactions with the steep bedrock and entrainment of basal material, or increased strain and compression of the ice flowing toward the nunatak, leading to particle aggregation and ice-crystal scale metamorphism (Baccolo, Delmonte, Di Stefano, et al., 2021). Dust concentrations portray attenuation with a lower variance and range of values compared to EDC. Although they both have a higher average value than EDC, the

https://doi.org/10.5194/egusphere-2026-2045
Preprint. Discussion started: 21 April 2026

ALHIC 2201 distribution shows a range of ~ 86% of EDC and ALHIC 2302 ~79% of EDC. Both cores display bimodal distributions but with differing dominant modes: ALHIC 2201 peaks at lower concentrations, whereas ALHIC 2302 peaks at higher values which is consistent with its proximity to the nunatak. In contrast, EDC exhibits a pyramidal-shaped distribution, highlighting the differences between site-specific dust dynamics between the East Antarctic interior and the Transantarctic Mountains margin.

The ALHIC water isotope values resemble those of other Victoria Land ice cores, such as Talos Dome, Taylor Dome, and S27 (Baggenstos et al., 2018; Crotti et al., 2022; Steig et al., 2000; Yan et al., 2021), reflecting the warmer site conditions than those of the East Antarctic interior, such as EDC (Table 1) (Landais et al., 2021). Both ALHIC 2201 and ALHIC 2302 exhibited lower average *d* in comparison to EDC, and ALHIC 2201 showed a particularly wide range, with values comparable to EDC (Fig. 4). These patterns of *d* may imply that the Allan Hills ice may incorporate material from multiple accumulation zones, such that the water isotope signal reflects a mixture of ice formed under different temperature and elevation conditions. Additionally, changes in sublimation and post-depositional regimes may have implications for interpreting water isotope data at this site (Hu et al., 2022). Neither ALHIC 2201 nor 2302 captures the full range of expected glacial–interglacial variability in δ^{18}O, with the range representing ~72% for ALHIC 2201 and ~45% for ALHIC 2302 to that of EDC (Fig. 6, Table 1).

Discrete analyses from the stratigraphically intact S27 core offers insight into the variance observed prior to stratigraphic disturbance (Yan et al., 2021). Comparing S27 and EDC δ^2H records of the same age range (~114-255 kyr), again, reveals distinct data distributions and variance patterns. After aligning the means (to account for regional differences) and binning the data into 250-year intervals, the δ^2H variance of S27 is ~77% that of EDC, possibly reflecting a smaller glacial-interglacial amplitude at Allan Hills compared to EDC. This may be a regional feature of Victoria Land as Talos Dome (TALDICE) (Crotti et al., 2022; Masson-Delmotte et al., 2008) and Taylor Dome (Steig et al., 2000) also exhibit smaller glacial-interglacial amplitudes than EDC (Table 1). This is further supported by the presence of two broad peaks in the S27 and TALDICE δ^2H distribution rather than three peaks as seen in the EDC (Fig. 9C and F). The reduced variance observed in the Allan Hills ice cores may therefore be partially attributed to regional characteristics of Victoria Land, rather than being solely a consequence of stratigraphic mixing or other post-depositional processes.

We speculate that signal-attenuating processes may be stronger at the ALHIC 2302 site due to its proximity to the nunatak, where steep bedrock topography likely promotes enhanced deformation, recrystallization, and mixing that alter the preserved climate signals. Dip angles resolved by three-dimensional multitrack electrical conductivity measurements (3D-ECM) find average dip angles of ~69° in ALHIC 2302 as compared to ~29° in ALHIC 2201 (Kirkpatrick et al., 2025). Ice coring straight down through dipping layers will result in those layers appearing to be thicker than when coring through layers that are parallel to the surface. A meter of ice core in steeply dipping ice (like at ALHIC 2302) will therefore have fewer layers than a meter of ice core in weakly dipping ice (like ALHIC 2201), which may contribute to the observed lower variance in the former core.

Similarly, during CFA analysis, melting ice perpendicular to the core axis while layers are inclined can over-represent the same layer, further reducing variance. The inclination of layers may cause multiple layers to be averaged or smoothed in CFA analysis, as the 2.7 cm wide melthead analytical surface can intersect several dipping layers at once, resulting in mixing, and thus smoothing, of the signals. This effect is likely stronger for $\delta^{18}O$ in ALHIC 2302, where the spatial resolution (~2.7 cm) is smaller than the smoothing imposed by melthead averaging (~7 cm, calculated as 2.7 cm × tan(69°)). In contrast, the smoothing effect for ALHIC 2201 would be ~1.5 cm (2.7 cm * tan (29°)). For CH_4, this effect is less pronounced, as its spatial resolution (~6 cm) is comparable to or larger than the smoothing length and is supported by no reduction in variance for ALHIC 2201 in comparison to EDC (Table 1).

The smaller age range in ALHIC 2302 may also be a contributing factor to the observed overall lower variance. The age range of ALHIC 2302 (303 ± 85 ka) is over three times narrower than that of ALHIC 2201 (1020 ± 85 ka), which may partly explain the lower variance observed in ALHIC 2302. Additionally, the first >1 Ma age is not sampled in ALHIC 2302 until > 125 m depth, whereas in ALHIC 2201, the first >1 Ma age is at 30 m, further supporting smaller age variability (and thus climate variability) in the ALHIC 2302 record.

Variable	**Dataset**	**Mean**	**Range**	**Variance**
CH_4	AH2201	557	407 – 719 (312)	8063
	AH2302	533	429 – 661 (232)	3574
	EDC	515	375 – 686 (311)	7459
Dust	AH2201	1.0×10^4	$1.1 \times 10^3 – 4.7 \times 10^4$ (4.5×10^4)	1.6×10^8
	AH2302	1.2×10^4	$2.5 \times 10^3 – 3.7 \times 10^4$ (3.4×10^4)	1.1×10^8
	EDC	7.3×10^3	$3.7 \times 10^2 – 4.0 \times 10^4$ (4.0×10^4)	1.3×10^8
$\delta^{18}O$	AH2201	-37.1	-39.9 – -34.4 (5.5)	2.2
	AH2302	-38.0	-39.5 – -36.1 (3.4)	0.9
	EDC	-53.3	-56.3 – -48.8 (7.6)	4.7
δ^2H	AH2201	-296.4	-318.9 – -271.4 (47.5)	157.9
	AH2302	-300.9	-314.1 – -284.3 (29.8)	58.9
	EDC	-417.9	-442.9 – -381.4 (61.5)	319.8
	S27	-326.1	-350.3 – -297.2 (53.1)	251.2
	EDC (S27)	-421.9	-441.2 – -379.3 (61.9)	325.0
	Talos Dome (S27)	-309.5	-328.1 – -275.8 (52.2)	228.5
	Taylor Dome (S27)	-309.7	-334.3 – -286.0 (48.3)	164.0
d	AH2201	0.73	-3.40 – 6.68 (10.08)	5.41
	AH2302	3.20	0.26 – 5.87 (5.61)	2.15
	EDC	8.44	5.42 – 11.53 (6.11)	2.67

Table 1. Summary statistics for each geochemical measurement — CH_4 (ppb), $\delta^{18}O$ (‰), δ^2H (‰), and d (‰) — for ALHIC 2201, ALHIC 2302, and EDC. For δ^2H, summary statistics are also shown for S27, EDC, Talos Dome, and Taylor Dome over the same time interval as the S27 record (denoted '(S27)'; ~114–152 kyr). Reported ranges correspond to the interval between the 2.5th and 97.5th percentiles. For Taylor Dome and Talos Dome, δ^2H values were not available for the age range of S27 and were calculated as $\delta^2H = 8 * \delta^{18}O + 10$.

3.3 Accumulation bias in the Allan Hills ice cores

Fundamentally, ice cores record environmental conditions only during times of snowfall, resulting in an inherent overrepresentation of periods with high accumulation rates, such as interglacials. In well-dated, stratigraphically continuous cores such as EDC, the over-representation of interglacial ice is accounted for via the depth-age scale. However, at Allan Hills, where stratigraphic discontinuities and averaging occur, this accumulation bias becomes problematic and complicates the interpretation of the snapshots that represent climate averages. Yan et al. (2021) estimated a 10-fold change in accumulation rate between glacial and interglacial periods at the Allan Hills (versus an approximately 2-fold change at interior sites), which could lead to substantial interglacial bias in the Allan Hills records.

3.3.1 Proportional representation of climate states

While the data distributions offer qualitative insight into how each measurement captures glacial–interglacial variability, they alone cannot determine which climate states are disproportionately represented. To address this, we applied a decile-based approach to assess potential accumulation and preservation biases. For each climate measurement, deciles were calculated for EDC (i.e., ten percentile bins, each representing 10% of the EDC data). These ranges were then used to bin the ALHIC data (after applying a mean offset for δ^{18}O and dust) into ten corresponding groups, and the proportion of ALHIC data within those ranges was calculated. For ALHIC cores, a proportion greater than 0.1 indicates more data in that value range relative to EDC, whereas a proportion less than 0.1 indicates relatively less data.

Evidence for interglacial bias in ALHIC ice is evident in that all three geochemical measurements exhibit a greater than expected (> 0.1) proportion of data in warmer climate ranges: higher CH_4 and δ^{18}O, and lower dust concentrations (Fig. 7). In some decile bins, there is roughly a doubling of expected data in warmer (i.e., interglacial) climatic values. Notably, for CH_4, a majority of the data—69% in ALHIC 2201 and 67% in ALHIC 2302—falls at or above the EDC median, reflecting a concentration of values toward the warmer part of the distribution. The δ^{18}O and dust data were aligned by their means to EDC to account for regional differences, making the use of the EDC median appropriate for comparison: 59% of ALHIC 2201 and 63% of ALHIC 2302 δ^{18}O values exceed the median, while dust concentrations show 47% and 53%, respectively. Complexities for interpreting Allan Hills dust records arise due to local deposition processes and potential particle aggregation from ice flow and recrystallization (Baccolo, Delmonte, Niles, et al., 2021).

The decile comparisons of Allan Hills S27 to EDC over the same time period (~114-255 kyr, binned by 1 m depth intervals) show proportionally more S27 data in the warmer δ^2H range, with 60% of values above the EDC median (Fig. 9B). The reduced variance and higher proportion of warmer δ^2H values mirror trends of our ALHIC 2201 and ALHIC 2302 CFA records, suggesting that these patterns may be derived from Allan Hills climatic and post-depositional regimes rather than solely stratigraphic disturbance. Some of these patterns may be attributed to regional climatic influences that differ from the interior at Dome C, such as Ross Sea influences on moisture transport (Scarchilli et al., 2011; Spaulding et al., 2013). Further, S27 layering may be tilted for the warm MIS 5 interglacial period (J. Marks-Peterson, personal communication), which would also result in its over-representation in the S27 core.

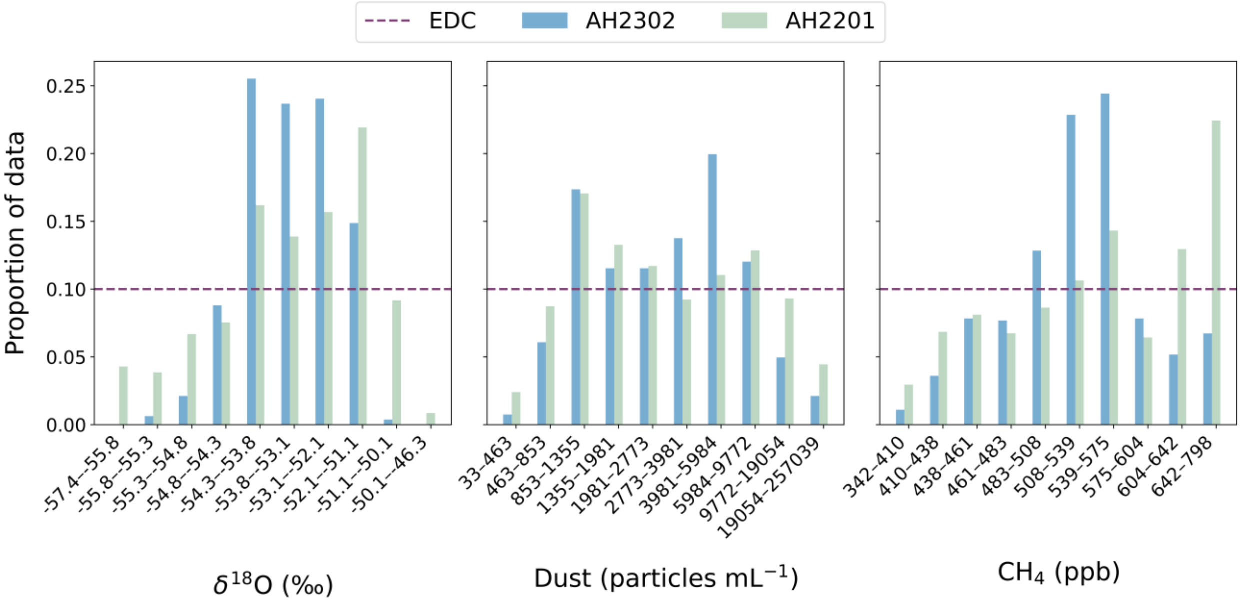

Figure 7. Decile comparison of ALHIC 2201 (green) and ALHIC 2302 (blue) to EDC (purple line, 10% by definition as EDC deciles were used to define bins) for $\delta^{18}O$ (left, per mil), dust concentrations (middle, particles mL^{-1}), and CH_4 (right, ppb). Mean offsets were applied to ALHIC $\delta^{18}O$ and dust as described in the caption of Figure 6. The minimum and maximum percentile bins include values that may be greater than what is shown (e.g., ALHIC 2201 has CH_4 values greater than 798 which is grouped in the maximum CH_4 decile bin).

3.3.2 Estimating glacial-interglacial accumulation contrast and signal smoothing

To interpret distributional differences between ALHIC and EDC, we generated artificial EDC records to approximate key processes likely affecting Allan Hills ice: interglacial accumulation bias and signal smoothing. Interglacial bias was simulated by preferentially resampling higher accumulation datapoints, and variance reduction was applied multiplicatively to mimic smoothing via mixing, diffusion, and thinning (see Appendix B for methods). Accumulation (α) and variance (k) scaling factors were applied to the EDC data distributions and optimized using the Wasserstein distance to match ALHIC distributions (Table B1). For ALHIC 2201 and 2302, α was estimated from $\delta^{18}O$ and applied to other geochemical measurements. We find that the observations constrain the variance scaling much more strongly than the accumulation scaling.

While the variance scaling is optimized for a narrow range of values in k, the accumulation scaling (α) produces multiple plausible solutions and should be interpreted with some caution. Despite these limitations, it is still meaningful in exploring potential biases. Our method assumes that if multiple glacial–interglacial cycles are adequately represented in ALHIC ice, the resulting artificial EDC distribution should converge toward the shape of the ALHIC distribution. Deviations between the artificial EDC and ALHIC distributions suggest the presence of sampling bias, likely driven by complex ice flow and stratigraphic disruption.

The scaling results reveal distinct behaviours in variance and accumulation adjustments between ALHIC 2201 and 2302 (Fig. 8, Table B1). Variance is well-constrained by the data: nearly all artificial EDC datasets required reduced variance to better match the ALHIC distributions, with ALHIC 2302 requiring smaller k values than ALHIC 2201 across all geochemical measurements, particularly $\delta^{18}O$ ($k = 0.42$ and 0.67, respectively). An exception is the artificial EDC CH_4 dataset matching the ALHIC 2201 CH_4 record, which required no variance scaling and already matches the EDC range (Table 1). In contrast, accumulation scaling produced contrasting results between ALHIC 2201 and 2302 while being overall less well constrained. For ALHIC 2302, an α of approximately 1 indicates that accumulation scaling (and thus interglacial bias adjustments) did not improve agreement between the EDC and ALHIC distributions. In other words, the ALHIC 2302 core appears more or less consistent with the glacial-interglacial accumulation contrast seen at EDC. However, ALHIC 2201 required an α of 3.8, which shifted the EDC distribution toward greater interglacial representation and warmer climate state values (Appendix B). The higher α corresponds to an increase in interglacial ice of ~50% (Table B1) and implies a near tripling of the IG-G accumulation rate ratio relative to the original EDC record (from ~2× to ~6×). Note that both estimates are smaller than the ten-fold IG-G accumulation contrast suggested by Yan et al. (2021).

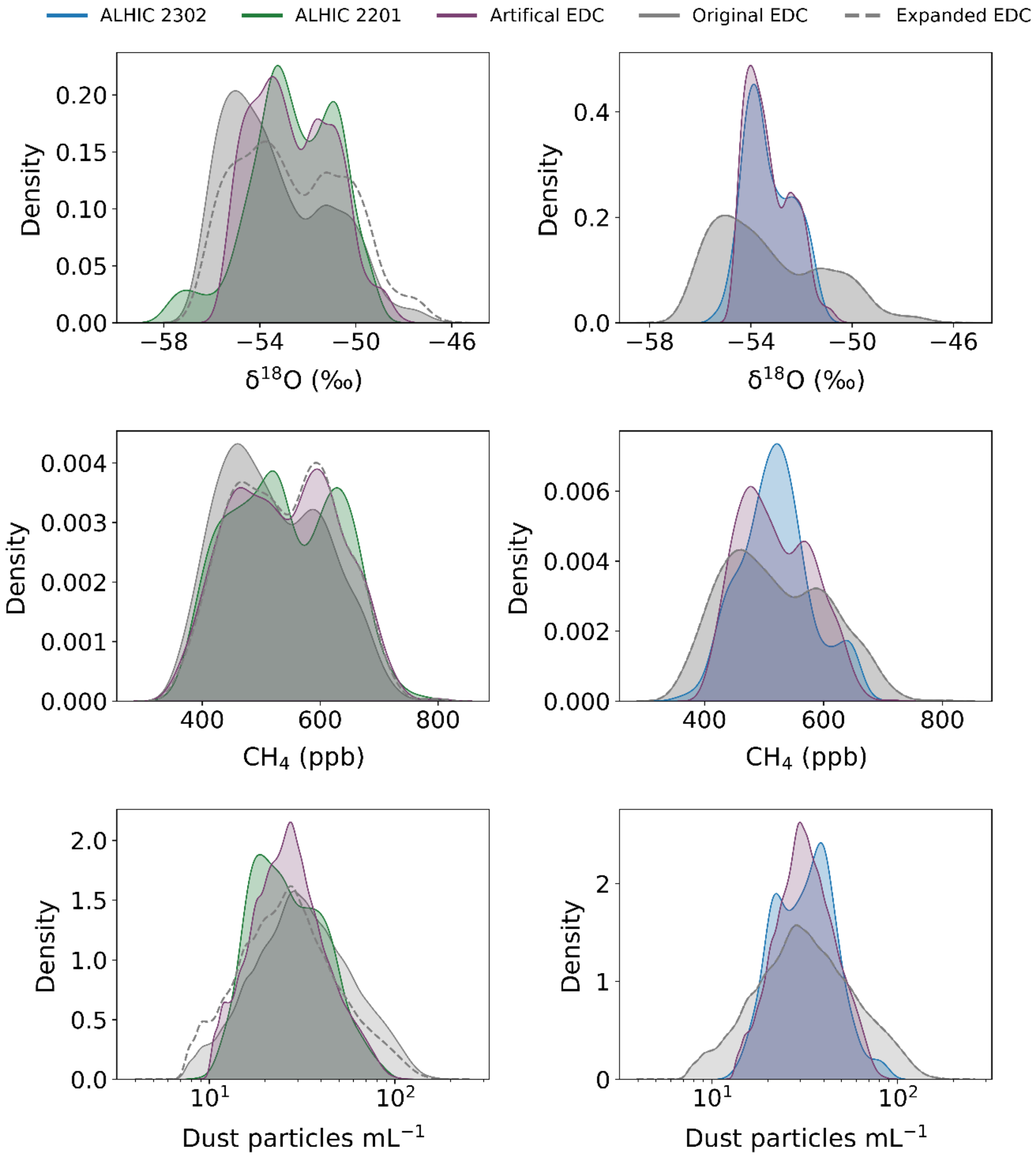

530

Figure 8. Artificial EDC KDE (purple) data distributions after applying the best-fit accumulation rate and variance scaling factors (i.e., applying α in Eq. B1 and *k* in Eq. B2). The dotted grey line shows the EDC data set after weighted resampling adjusting for accumulation rate and the grey KDE distribution is the original, unmodified EDC distribution. The ALHIC 2201 and ALHIC 2302 distributions are green (left) and blue (right), respectively. Mean offsets are applied initially to the ALHIC records of $\delta^{18}O$, and applied after scaling to $\delta^{18}O$, dust, and CH_4 concentrations. 535

https://doi.org/10.5194/egusphere-2026-2045
Preprint. Discussion started: 21 April 2026

These patterns point to underlying differences in how climate signals are preserved within the ALHIC archive. Reduced variance is apparent in both records, but more pronounced in ALHIC 2302. Interglacial bias is more evident in ALHIC 2201, although accumulation dynamics are still not well-constrained and further geochemical work should be done to explore accumulation rates thorough time at the Allan Hills. The lower accumulation scaling factors (α) for ALHIC 2302 and smaller variance scaling factors (k) suggest that these distributional differences between ALHIC 2302 and EDC are predominantly driven by variance reduction and signal smoothing processes. These observations may suggest that the degree of interglacial bias may vary through the Allan Hills blue ice archive, perhaps reflecting spatial patterns in the IG-G accumulation contrast in the regions that source the modern ice field. Interestingly, the two sites compared here suggest a pattern in which records recovered from drill sites with high degrees of smoothing reveal less interglacial bias than those that experience less smoothing. These observations are consistent with the findings of only long snapshots in ALHIC 1902 (nearby ALHIC 2302) and short snapshots inferred in shallower layers in ALHIC 1901 (nearby 2201) (discussed further in Section 3.4) (Marks-Peterson et al., 2026; Shackleton et al., 2025, 2026). Whether this is a systematic pattern or just a coincidence remains to be seen.

The presence of reduced variance and interglacial bias in a stratigraphically intact core, S27, suggests that these features in the Allan Hills record arise prior to stratigraphic mixing. Applying the accumulation scaling factor derived from ALHIC 2201 $\delta^{18}O$ (justified by its similar location within the Allan Hills ice field) to the EDC record over the same age range as S27 (binned at 1 m depth intervals) yields a variance scaling factor of $k = 0.78$ for δ^2H (Fig. 9F). The artificial EDC distribution shows a reduced peak at colder values and an increase in density at warmer values. This shift is consistent with enhanced preservation of interglacial conditions under higher accumulation rates.

To assess potential regional precipitation effects of Victoria Land relative to Dome C, the same approach was applied to TALDICE δ^2H record over the S27 age range (binned at 1 m intervals). The best-fit parameters ($\alpha = 0.3$, $k = 0.9$) suggest fundamentally different accumulation dynamics compared to both EDC and the Allan Hills (Fig. 9). Unlike S27, TALDICE requires downscaling of higher-accumulation intervals in EDC (i.e., $\alpha < 1$), indicating that such intervals are overrepresented in EDC relative to TALDICE and colder, low-accumulation intervals are overrepresented (Fig. 9E-F). Variance reduction is minimal and consistent with the TALDICE standard deviation being ~84% of that of EDC over the same interval (Table 1).

Although both TALDICE and the Allan Hills are in Victoria Land, these results highlight potential regional differences in accumulation sensitivity across glacial cycles. In southern Victoria Land, where the Allan Hills are located, accumulation variability may be strongly influenced by changes in Ross Ice Shelf extent and shifts in synoptic storm tracks, contributing to the larger interglacial–glacial accumulation ratio observed at the Allan Hills compared to TALDICE (Table B1) (Morse 1998, Yan 2021, Aarons 2016; Carter 2026). The TALDICE chronology (despite its lower temporal resolution than EDC) suggests

https://doi.org/10.5194/egusphere-2026-2045
Preprint. Discussion started: 21 April 2026

an IG-G accumulation ratio of 1.40, which is more comparable to EDC (1.85) and lower than that inferred for ALHIC 2201 $\delta^{18}O$ (5.9), and nearly identical to our estimate of IG-G after applying accumulation and variance scaling factors (Table B1).

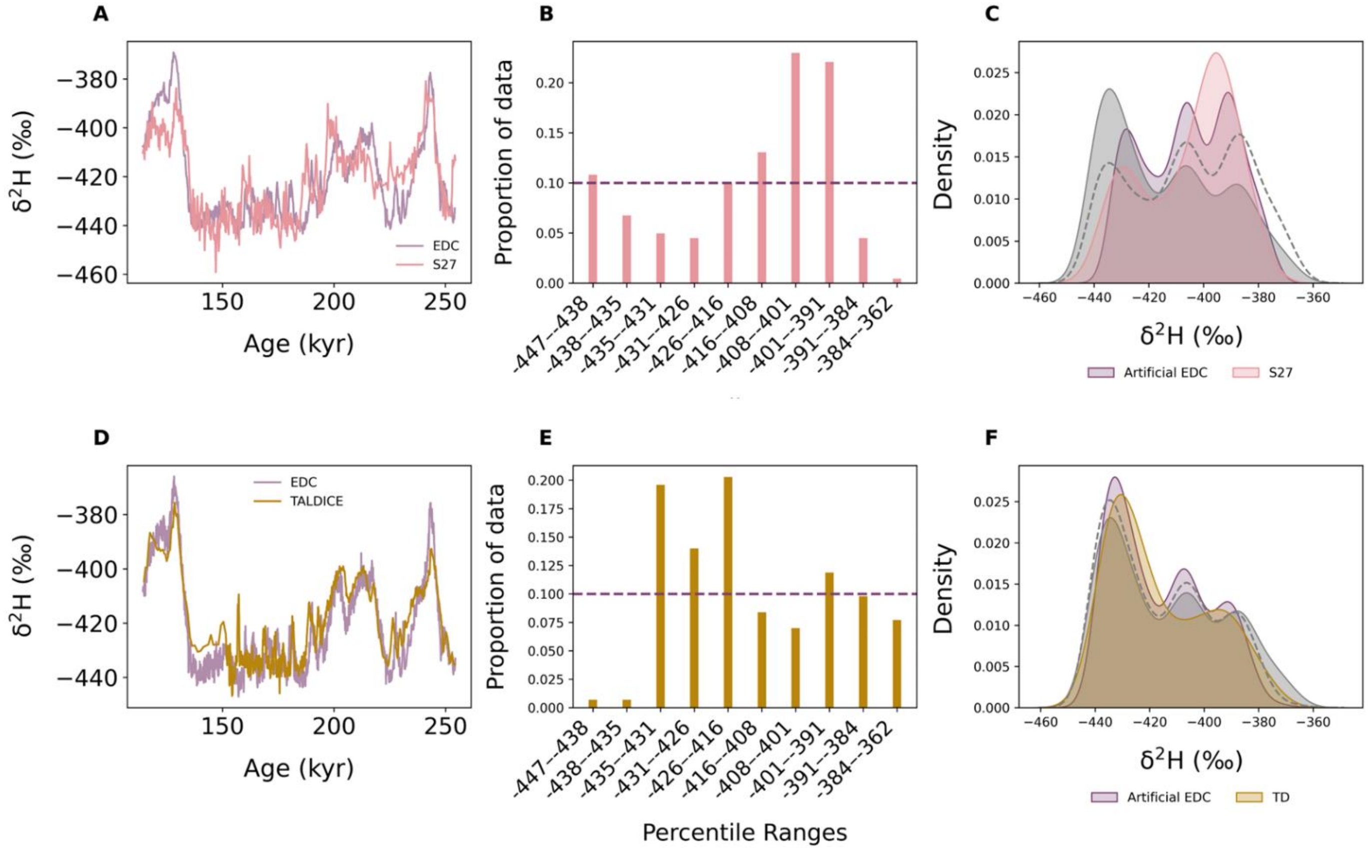

Figure 9. Comparison of S27 (pink), TALDICE (gold), and EDC (purple) of the same period (~114-254 kyr). A mean offset was applied to the S27 and TALDICE δ^2H values due to regional climatic differences. (A, D) The aligned S27 and TALDICE compared to the EDC δ^2H records. (B, E): The deciles of the S27 and TALDICE data compared to EDC (purple line, 10% by definition as EDC deciles were used to define bins). (C, F): Artificial EDC KDE (purple) data distributions after applying an accumulation rate (α) and variance scaling (k) factors. The dotted grey line shows the EDC data set after adjusting for accumulation rate (applying α) and the grey KDE distribution is the original EDC distribution. An offset was subtracted from the S27 and TALDICE δ^2H record to align the mean to EDC.

3.4 Signal preservation throughout the ice column

Signal attenuation and averaging effects are more pronounced with depth as evidenced by the transition to only long snapshots below 140 m in ALHIC 1901 (Marks-Peterson et al., 2026). Comparing our ALHIC 2201 and 2302 continuous records to deeper discretely-measured records, as well as to neighbouring boreholes where very old ice has been discovered, can help contextualize our ALHIC CFA and discrete records in terms of glacial-interglacial variability and old ice preservation. ALHIC

1902, located ~30 m upstream (in deeper ice) from ALHIC 2302, has yielded the oldest ice to date (~6 Ma, Shackleton et al., 2025), while ALHIC 1901, located ~100 m from ALHIC 2201, has recovered ice up to ~4 Ma (Shackleton et al., 2025). The maximum ages estimated for ALHIC 2302 and ALHIC 2201 are ~6.5 and ~2.8 Ma (Higgins et al., 2026) respectively, occurring near the bed and outside of the CFA analyses depths.

Our observed differences in signal variance between ALHIC 2201 and 2302 are consistent with earlier assessments of short and long snapshots, which exhibit relatively high and low variance, respectively. Reduced variability with depth is particularly evident in ALHIC 2302; the neighbouring core ALHIC 1902 did not show any short snapshots in Marks-Peterson et al. (2026). Conversely, ALHIC 2201 CFA exhibits higher variability at shallower depths, consistent with short snapshots observed above 140 m in the neighbouring core ALHIC 1901.

Combining the CFA data with the previously analysed discrete $\delta^{18}O$ measurements that include deeper sections of ALHIC 2201 and 2302 allows for assessment of variance throughout the ice column and for comparison to neighbouring and more distant cores (Fig. 10). We plot the data as a function of distance from the bed to account for differences in ice thickness, given that the oldest ice is systematically found within a narrow basal unit at the bed rather than at a fixed depth from the surface. We grouped ALHIC 2302 with 1902 and ALHIC 2201 with 1901, given their proximity (Fig. 1). The CFA and discrete water isotope data for the paired cores were combined and binned into 10 m depth intervals to calculate variances.

https://doi.org/10.5194/egusphere-2026-2045
Preprint. Discussion started: 21 April 2026

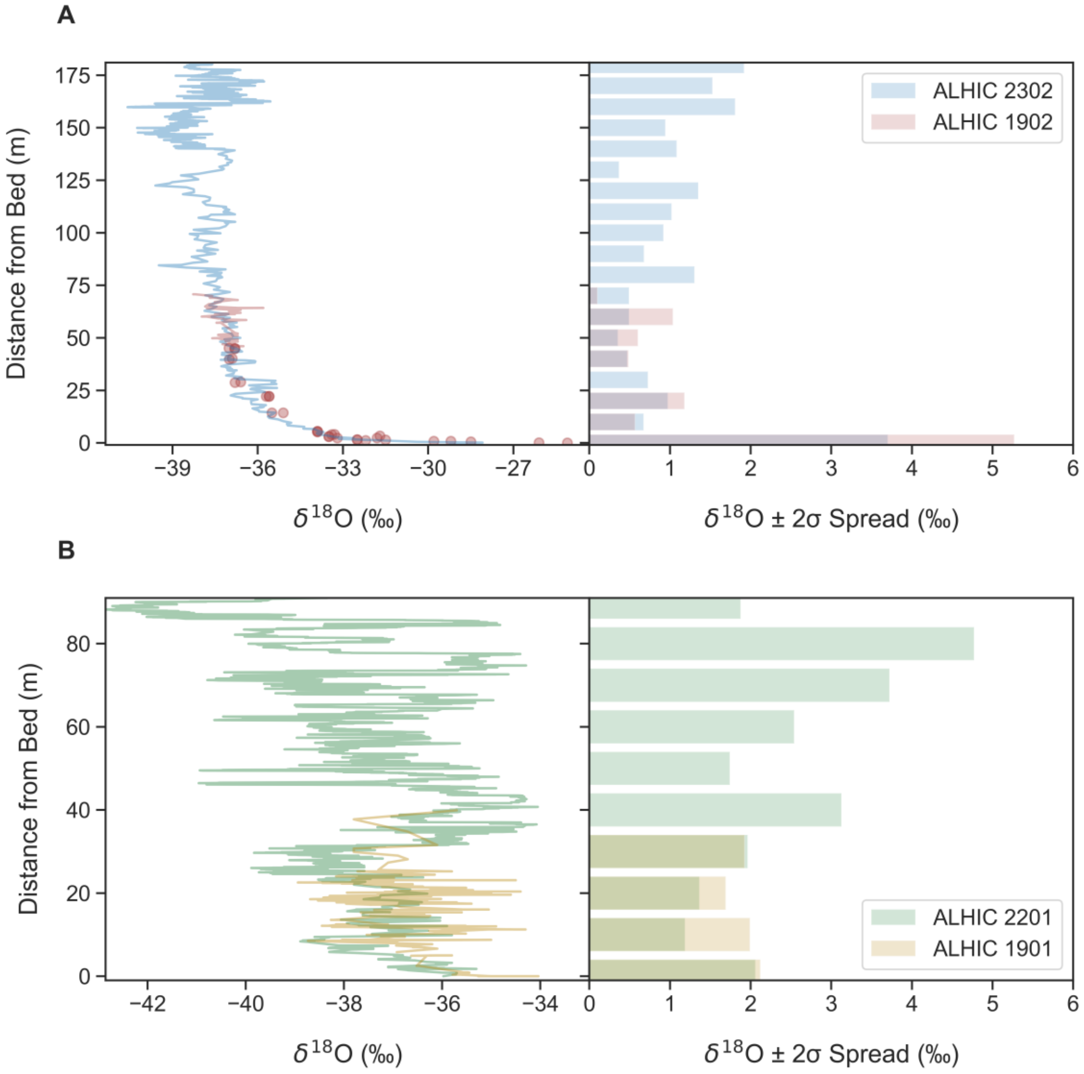

605 **Figure 10. Comparison of δ^{18}O profiles (left) and two standard deviations of the mean (right) across neighbouring ALHIC ice cores for 10 m binned depths as a function of distance from bed (m). A: ALHIC 2302 (blue) and 1902 (red). B: ALHIC 2201 (green) and 1901 (yellow).**

This comparison shows two key patterns: 1) variance generally decreases with depth, and 2) ALHIC 2302/1902 exhibit less 610 variance throughout the entire ice column than ALHIC 2201/1901 do; the exception being the bottom ~20 m where the large δ^{18}O range in ALHIC 2302/1901 represents the secular climatic cooling trend over the wide range of preserved ages, rather than signal variance (~2.5 to > 6 Ma, where δ^{18}O is strongly correlated with age). The mean standard deviations (± 2σ) for

ALHIC 2302/1902 across all 10 m bins are roughly half those of ALHIC 2201/1901 (~1 versus ~2 ‰). Aside from the top and bottom bins of ALHIC 2302/1902, most binned intervals exhibit standard deviations below 2 ‰, whereas 57 % of the ALHIC 2201/1901 depth bins exceed 2 ‰. These differences further support the hypothesis that ice cores near the nunatak are influenced by processes that reduce glacial–interglacial preservation. Moreover, the proximity to the nunatak may be responsible for trapping very old ice near bedrock as evidenced by ^{40}Ar basal ice ages in these cores, which are over 2 Ma older than those from ALHIC 2201/1901.

These patterns underscore the influence of core location and depth in the Allan Hills and their implications for paleoclimate interpretations. There is an apparent trade-off between very old ice preserved near the nunatak and the reduced glacial-interglacial variability (i.e., all long snapshots) caused by enhanced signal attenuation processes. Conversely, ice cores located closer to the MIF flow line may retain more glacial-interglacial variability, reflecting higher signal fidelity (i.e., short snapshots). Ultimately, more high-resolution data are needed on older and deeper samples to better interpret stratigraphy and variance. Future drilling at the Allan Hills or in other blue ice areas will require investigation of each location's unique fidelity of the archive, as even cores separated only a few kilometres are heavily influenced by local topography and ice flow dynamics that have implications for interpreting climate records.

Conclusions

The Allan Hills blue ice area contains a trove of old ice that is currently our best option for extending climate records into enigmatic, older climate periods beyond our continuous ice core records. However, ice flow and deformation near the ice sheet margin causes stratigraphic disturbances that create challenges unique to blue ice areas, warranting continued investigations into the fidelity of the climate archive. High-resolution measurements of methane, water isotopes, and dust allow us to quantitatively and qualitatively assess these complexities. Continuous Flow Analysis (CFA) on two shallow ALHIC cores, 2201 and 2302, combined with ^{40}Ar dating revealed disturbed stratigraphy and meter-scale folding in ALHIC cores. Our analyses confirmed the reduced glacial-interglacial variability and interglacial bias as well as characterized multiple geochemical measurements in Allan Hills ice. These findings further our understanding of the potential and complexities of blue ice areas as a paleoclimate archive.

Deeper and older ice likely experiences even stronger climate signal attenuation as shown in discretely measured records form the Allan Hills (Marks-Peterson et al., 2026; Shackleton et al., 2025, 2026). Further high-resolution analyses should be prioritized at depth as ice quality improves with improved drilling techniques, for example, by use of drilling fluid. Completing CFA analyses at greater depths and on older ice will help interpret measurements that must be measured discretely, such as CO_2, that are integral to our understanding of key climate dynamics, by better understanding its relationship with variance, depth, and ice age. Future and ongoing projects will aim to integrate various analytical techniques—including CFA, 3D-ECM, 645 discrete analyses, and ^{40}Ar dating to further resolve the complex stratigraphic patterns observed. Together, these diverse toolsets will improve our understanding of the valuable and unique paleoclimate archive discovered at Allan Hills.

Appendix A

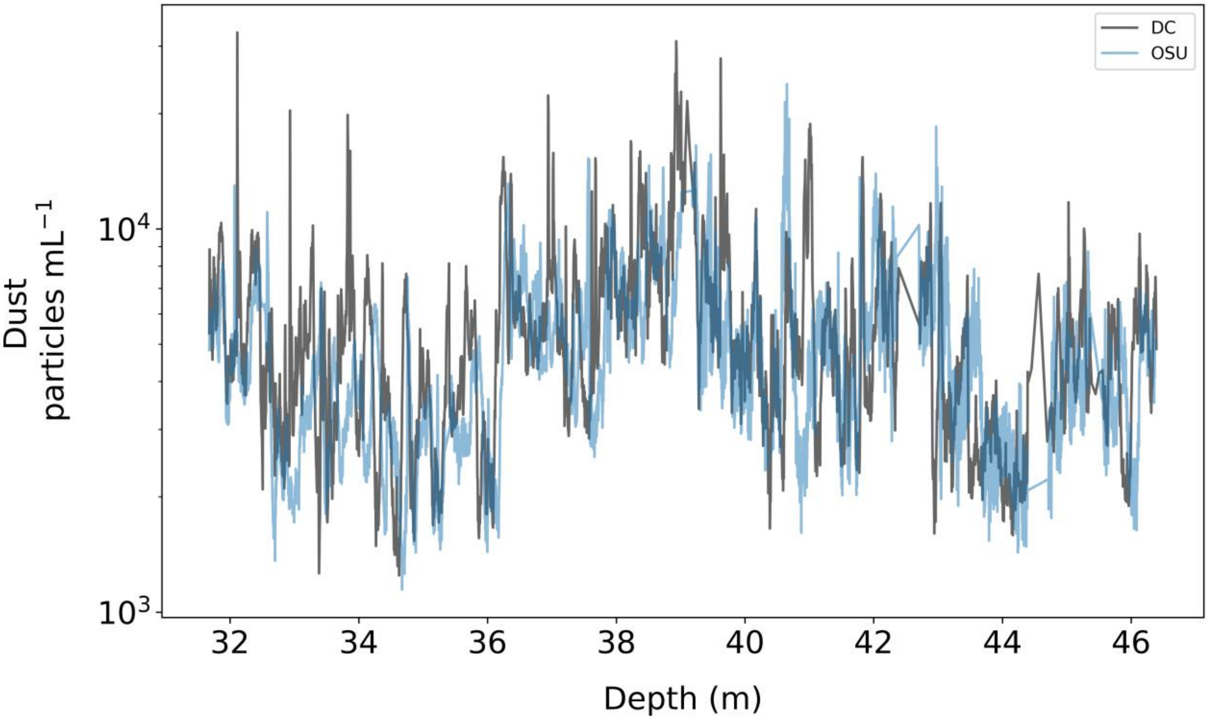

Figure A1. Dust concentration (particles mL^{-1}) comparison for ALHIC 2302 between Oregon State University (OSU, blue) data and 650 Dartmouth College (DC, grey). Differences in Abakus instruments and particle size bin widths between labs were accounted for by using bins between ≥1 µm and <10 µm for concentration calculations. Overall differences in variability may result from depth alignment differences, stratigraphic offsets, variability across the ice core slab, sensitives between Abakus instruments, or different laboratory designs.

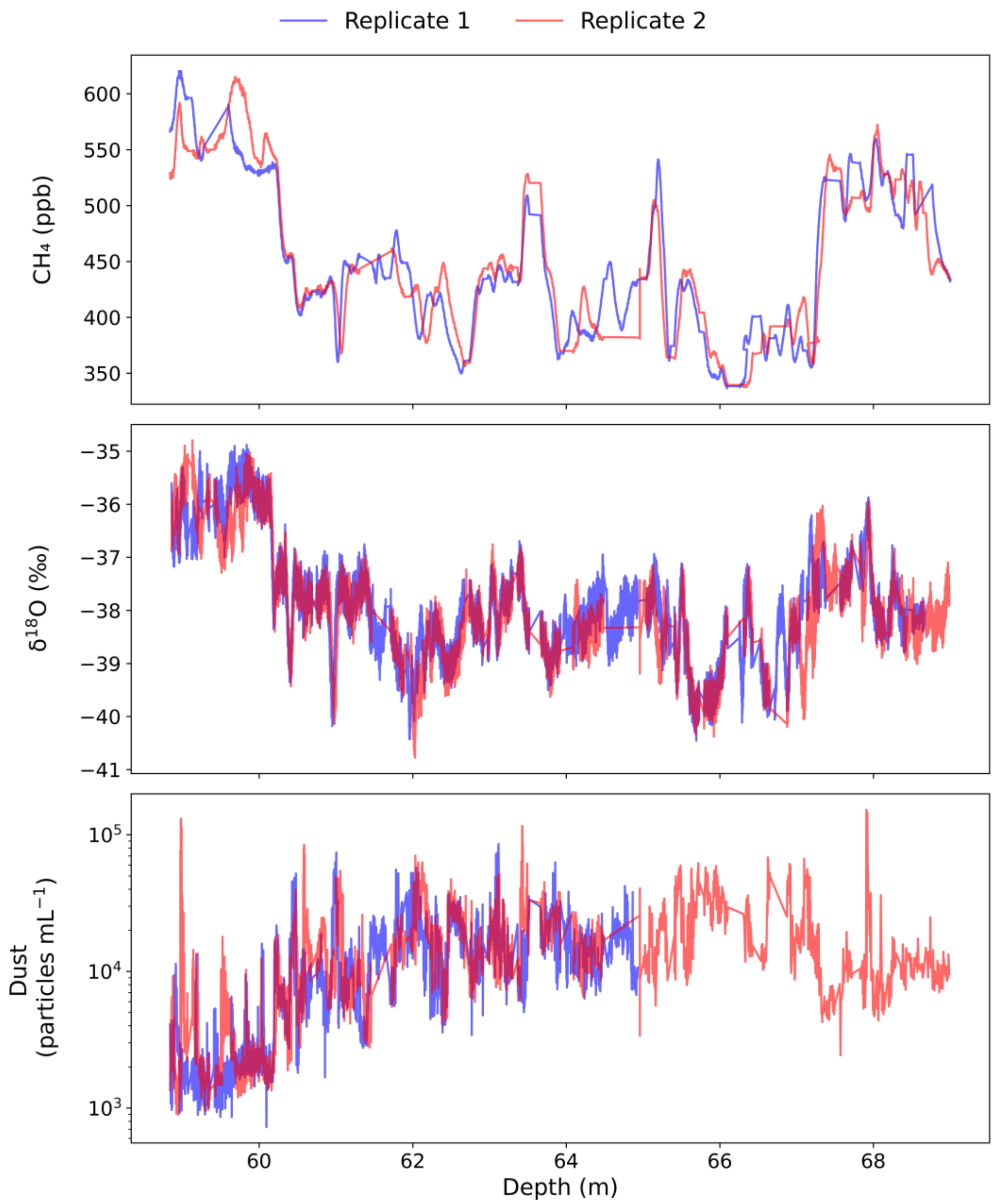

655 **Figure A2. Replication datasets for ALHIC 2201 for CH_4 (top, ppb), $\delta^{18}O$ (middle, per mil), and dust concentrations (bottom, particles mL^{-1}). Replicates 1 and 2 are shown in blue and red, respectively. Dust concentrations for depths ~65-69 m in the replicate core were not captured due to a software error and therefore these data are missing.**

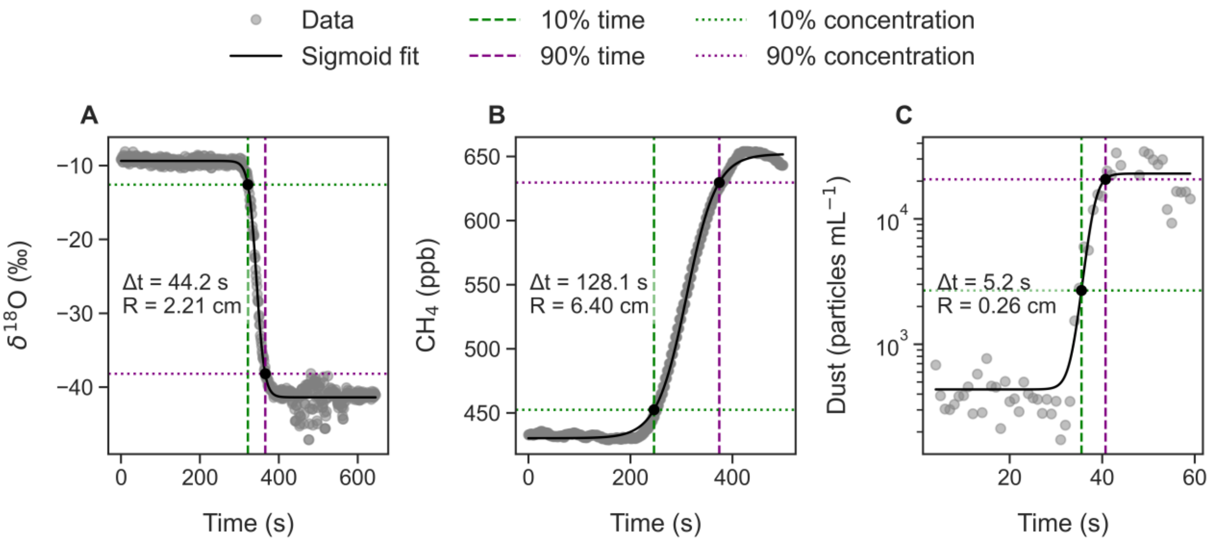

660

Figure A3. Response times (Δt) and resolution (R) for each analytical system: A) δ^{18}O, B) CH$_4$, and C) dust. δ^{18}O and dust data were calculated from the concentration changes between Milli-Q water and Taylor Glacier ice, while CH$_4$ data were derived from glacial and interglacial ice from Taylor Glacier. Resolution (R) is calculated as the transition time (Δt, defined as the time for a 10–90% concentration change) multiplied by the average melt rate (3 cm min^{-1}).

665

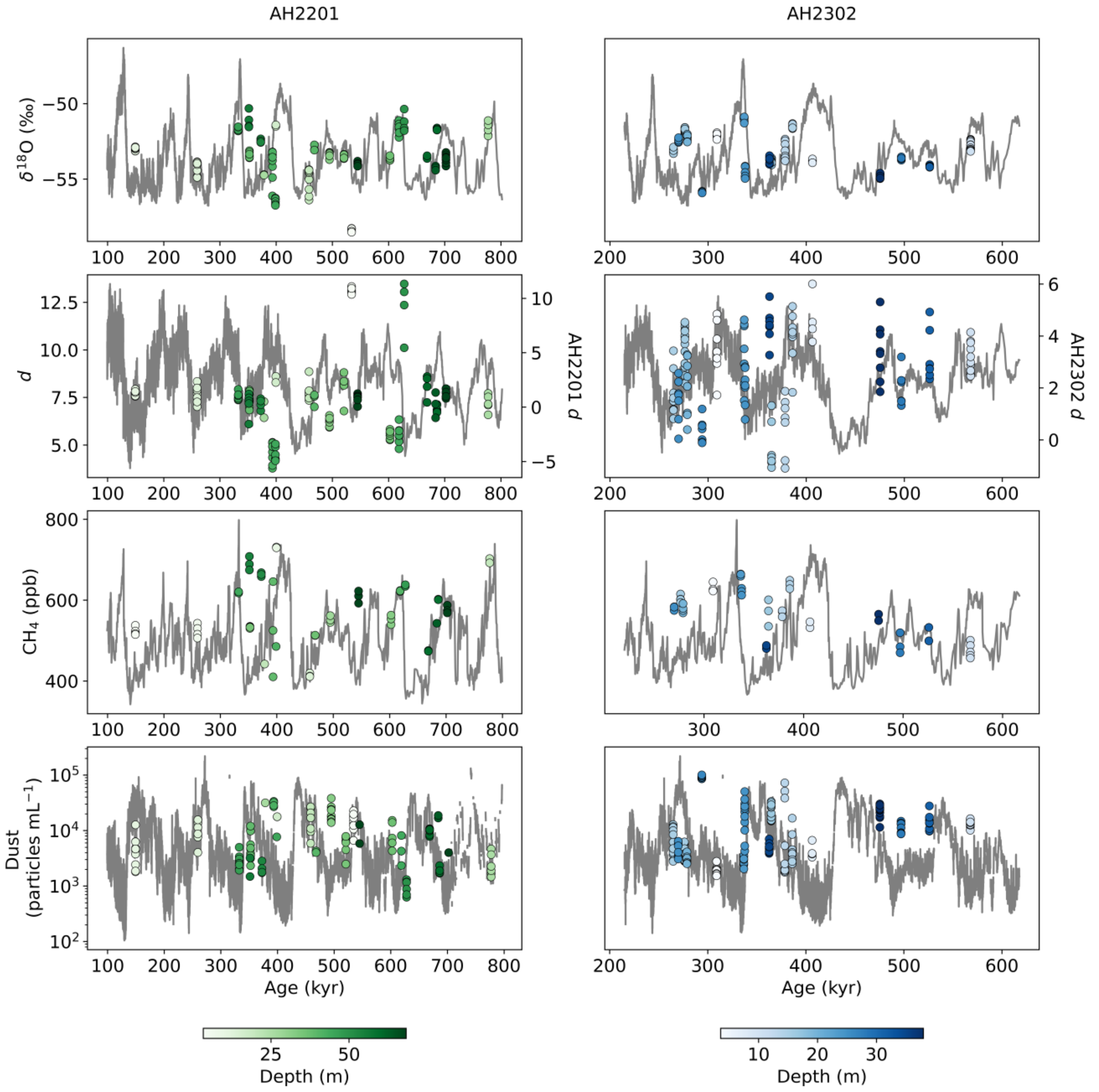

Figure A4. Comparison of ALHIC 2201 (left) and ALHIC 2302 (right) records overlayed on EDC. Rows show δ^{18}O (‰) (with a mean offset on the CFA data), *d* (EDC on left axis and ALHIC on right axis), CH$_4$ (ppb), and dust concentration (particles mL^{-1}). Scatter points represent the dated ALHIC data (sampled at the same depth intervals as the ^{40}Ar measurements) and are colored by depth within each core. ALHIC δ^{18}O, *d*, and dust data are plotted using their respective spatial resolution scales to include more data points (e.g., δ^{18}O measurements every 2 cm, dust. ALHIC dust concentrations are subsampled at every 1.25 cm and EDC dust concentrations are smoothed using a 15-point rolling mean for visual clarity.

Dataset	x	y	r	R^2	slope	intercept	R 95% CI	p	Std error
ALHIC 2201	CH_4	Dust	-0.66	0.44	0.00	5.24	-0.7, -0.63	< 0.001	0
	CH_4	*d*	0.17	0.03	0.00	5.71	0.11, 0.22	< 0.001	0
	$\delta^{18}O$	$\delta^{2}H$	0.98	0.97	7.81	-1.84	0.98, 0.98	< 0.001	0.04
	$\delta^{18}O$	CH_4	0.77	0.59	47.84	3089.80	0.74, 0.79	< 0.001	1.3
	$\delta^{18}O$	Dust	-0.68	0.47	-0.17	-5.52	-0.71, -0.65	< 0.001	0.01
	$\delta^{18}O$	*d*	-0.13	0.02	-0.19	-1.84	-0.21, -0.04	< 0.001	0.04
	$\delta^{2}H$	CH_4	0.75	0.56	5.47	2828.54	0.72, 0.77	< 0.001	0.16
	$\delta^{2}H$	Dust	-0.72	0.52	-0.02	-5.88	-0.75, -0.69	< 0.001	0
	$\delta^{2}H$	*d*	0.06	0.00	0.01	13.04	-0.02, 0.14	0.041	0.01
	Dust	*d*	-0.17	0.03	-1.04	12.02	-0.23, -0.11	< 0.001	0.17
ALHIC 2302	CH_4	Dust	-0.46	0.21	0.00	4.84	-0.51, -0.39	< 0.001	0
	CH_4	*d*	0.22	0.05	0.01	5.81	0.16, 0.28	< 0.001	0
	$\delta^{18}O$	$\delta^{2}H$	0.98	0.96	7.75	-5.08	0.97, 0.98	< 0.001	0.06
	$\delta^{18}O$	CH_4	0.53	0.28	33.54	2323.29	0.46, 0.6	< 0.001	2.11
	$\delta^{18}O$	Dust	-0.66	0.44	-0.26	-10.26	-0.7, -0.62	< 0.001	0.01
	$\delta^{18}O$	*d*	-0.15	0.02	-0.25	-5.08	-0.21, -0.08	< 0.001	0.06
	$\delta^{2}H$	CH_4	0.57	0.32	4.43	2386.19	0.5, 0.63	< 0.001	0.25
	$\delta^{2}H$	Dust	-0.70	0.49	-0.03	-10.95	-0.73, -0.67	< 0.001	0
	$\delta^{2}H$	*d*	0.06	0.00	0.01	14.14	0, 0.12	0.071	0.01
	Dust	*d*	-0.16	0.03	-0.70	10.86	-0.24, -0.08	< 0.001	0.15
EDC	CH_4	Dust	-0.67	0.45	0.00	5.88	-0.7, -0.64	< 0.001	0
	CH_4	*d*	0.22	0.05	0.00	6.42	0.17, 0.26	< 0.001	0
	$\delta^{18}O$	$\delta^{2}H$	1.00	0.99	8.14	15.82	1, 1	< 0.001	0.02
	$\delta^{18}O$	CH_4	0.77	0.60	29.77	2096.30	0.75, 0.8	< 0.001	0.65
	$\delta^{18}O$	Dust	-0.85	0.72	-0.22	-8.46	-0.86, -0.83	< 0.001	0
	$\delta^{18}O$	*d*	0.18	0.03	0.14	15.82	0.13, 0.22	< 0.001	0.02
	$\delta^{2}H$	CH_4	0.78	0.61	3.66	2040.17	0.76, 0.8	< 0.001	0.08
	$\delta^{2}H$	Dust	-0.86	0.74	-0.03	-8.15	-0.87, -0.85	< 0.001	0
	$\delta^{2}H$	*d*	0.27	0.07	0.02	19.04	0.22, 0.31	< 0.001	0
	Dust	*d*	-0.33	0.11	-0.94	11.94	-0.37, -0.28	< 0.001	0.07

Table A1. Summary statistics of Pearson correlations (r) for each geochemical measurement for ALHIC 2201, ALHIC 2302, and EDC. The EDC dataset was binned at a 1 m scale and was randomly sampled to n = 1000 to account for the differences in sample sizes between the EDC and ALHIC datasets. Dust concentration used for these estimates is the $\log_{10}$ of the concentration. The p-values were estimated with bootstrapping for 1000 iterations with full sample replacement to account for large same sizes.

Appendix B

To investigate the potential drivers of the observed distributional differences between EDC and ALHIC, we created artificial EDC datasets impacted by smoothing and accumulation bias. We applied a weighted resampling method to the EDC datasets that was used to simulate an interglacial bias. Each EDC datapoint is assigned a weight, β_i, based on the associated EDC accumulation rate, a_i, from the AICC2023 chronology. The weight, β_i, is scaled linearly by an accumulation factor (α):

$$\beta_i = 1 + (\alpha - 1) * (a_i - a_{min})/(a_{max} - a_{min}), \tag{B1}$$

where $amin$ and $amax$ are the minimum and maximum EDC accumulation rate, respectively. Next, we randomly resample from the EDC dataset, where the probability of drawing a given datapoint is scaled to β_i. The probability of a datapoint to be sampled is equal to the weight of the datapoint divided by the sum of all the weights in the dataset to ensure the sum of all probabilities approximately equals 1. When α=1, all datapoints are weighted equally in the drawing and the artificial distribution is identical to the original EDC distribution. When α>1, datapoints with higher accumulation rates are more likely to be sampled, with the probability proportional to their weight; conversely, when $\alpha < 1$, datapoints with higher accumulation are less likely to be sampled. For example, when α=10, datapoints at the maximum accumulation rate are ten times more likely to be sampled than those at the minimum, with all intermediate values scaled proportionally. The number of datapoints sampled for the distribution is equal to the integer of the sum of all the weights (therefore, the sample size increases with higher α). Thus, the resampled dataset is inflated for high-accumulation points when α>1. We test 50 values of α between 0.5 and 12 in equal steps.

To account for signal attenuating processes in Allan Hills ice, the EDC datapoints are multiplicatively scaled. Scaling factors, k, were defined from observed variance differences between the datasets, with 50 linearly spaced values ± 0.3 around the ratio of standard deviations between ALHIC and EDC. The scaled data, X_{scaled}, is defined as:

$$X_{scaled} = \bar{X}_{EDC} + k(X - \bar{X}_{EDC}), \tag{B2}$$

where $\bar{X}_{EDC}$ is the mean EDC value and X is the original value. This scaling reduces the variance by a factor of k^2 and the standard deviation by a factor of k, while preserving the mean.

Each combination of accumulation-rate scaling factors (α) and variance scaling factors (k) are applied to the EDC dataset and the distributions (artificial EDC and ALHIC) are quantitively compared using the minimum Wasserstein distance (also known as earth mover's distance). This metric measures the 'cost' required to transform one distribution into another by multiplying the amount of probability mass moved by the distance it is moved. Mean offsets are applied for $\delta^{18}O$, dust, and CH_4 to prevent bias in the Wasserstein distance and solely evaluate the shapes of the data distributions. The lowest 5% of cost estimates were assigned a weight to emphasize lower costs (i.e., best distributional matches) and used to report a 95% confidence interval (Table B1).

Out of the three variables, the accumulation scaling factor for $\delta^{18}O$ is s the most reliable geochemical measurement for this analysis in that CH_4 may be affected by in situ microbial production or laboratory air contamination, and dust is influenced by local sources and bedrock interactions, complicating interpretations of distributional differences. For this analysis, ALHIC 2201 depths with d values greater than 5 are excluded from the analysis, as these are associated with the coldest values in the record and the low-density mode in the distribution, that ultimately heavily penalized the Wasserstein distance cost estimate. This packet of ice is likely derived from a different origin as indicated by the cold values and high *d* associated with higher elevation sites. Excluding these data allowed the ALHIC 2201 δ^{18}O cost landscape to reveal a clear centroid of low-cost values rather than a valley, providing a meaningful α solution for accumulation scaling.

To further assess the degree of interglacial bias, we evaluated the percent change of interglacial ice in the artificial dataset from the original. We defined interglacial samples as datapoints within a defined Marine Isotope Stage (MIS) interglacial period (e.g., MIS 7) that also had an accumulation rate above the 90th percentile of glacial period accumulation rates. This criterion was chosen because MIS interglacial stages are defined at the onset of a glacial termination, when accumulation rates are still low and the climate state remains glacial. Using the EDC AICC2023 chronology, we define both the interglacial-glacial (IG-G) accumulation rate ratio and the fraction of interglacial ice (Table B1). The IG-G ratio is calculated as the ratio of the 75th percentile of interglacial accumulation rates to the 25th percentile of glacial accumulation rates, capturing the fold change between climatic states. The resulting normalized frequency accumulation rates and relative change in accumulation rates to the artificial EDC datasets are shown for the δ^{18}O datasets for ALHIC 2302 and the reduced ALHIC 2201 in Fig. B1.

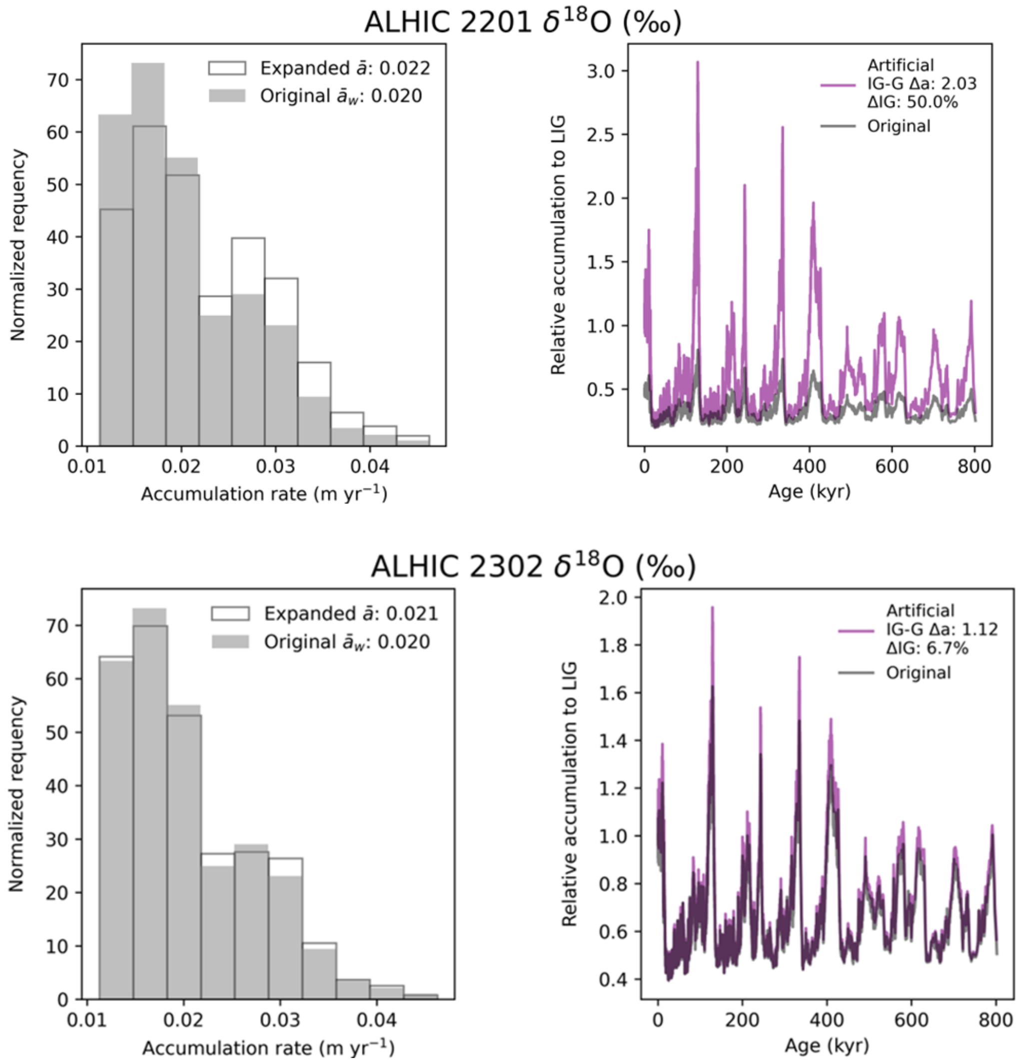

Figure B1. Comparison of EDC δ^{18}O accumulation characteristics before and after accumulation scaling to ALHIC 2201 and 2302. Left: Histograms of accumulation rates for the expanded dataset after applying α (open grey) versus the original dataset (filled grey), normalized so that the total area equals 1. Mean accumulation rates for the original and expanded datasets are indicated as $\bar{a}$ and $\bar{a}_w$, respectively. Right: Time series of accumulation rates relative to the Last Interglacial (LIG; 130–115 kyr), showing the expanded (purple) dataset with accumulation rate multiplied by the weight (β_i) and the original accumulation rate (grey). Percent change of interglacial ice in the dataset from the original to the expanded is denoted as ΔIG and the and the interglacial-glacial accumulation ratio change relative to the original data set is denoted as IG-G Δa in the legend.

Dataset	IG-G	ΔIG-G	ΔIG	α	α CI	*k*	*k* CI
EDC	2.09						
EDC (S27 ages)	1.85						
TALDICE	1.4						
ALHIC 2302 $\delta^{18}O$	2.34	1.12	5.92	**1.2**	+2.48/−1.51	0.42	+0.06/−0.05
ALHIC 2201 $\delta^{18}O$	5.85	2.8	50.48	7.07	+3.49/−3.78	0.73	+0.03/−0.03
ALHIC 2201 (reduced) $\delta^{18}O$	4.25	2.03	34.57	**3.79**	+2.87/−2.53	0.67	+0.03/−0.04
ALHIC 2201 CH_4	7.09	3.39	63.6	10.12	+1.55/−1.97	1.03	+0.04/−0.04
ALHIC 2302 CH_4	1.5	0.72	-14.18	0.5	+1.62/−1.67	0.7	+0.10/−0.08
ALHIC 2201 dust	4.1	1.96	32.68	3.32	+5.50/−3.89	0.75	+0.05/−0.05
ALHIC 2302 dust	4.1	1.96	32.68	3.32	+5.58/−5.92	0.6	+0.03/−0.04
S27 δ^2H	9.27	4.43	96.89	10.59	+1.91/−2.31	0.78	+0.04/−0.05
TALDICE δ^2H	1.38	0.66	-22.7	0.3	+0.60/−0.40	0.9	+0.13/−0.09

Table B1. Best-fit accumulation (α) and variance scaling (*k*) factors applied to EDC $\delta^{18}O$, CH_4, and dust records, selected as the minimum the Wasserstein distance to the respective ALHIC target distribution. The best fit α for $\delta^{18}O$ for ALHIC 2302 and ALHIC 2201 with high *d* values removed (denoted as 'reduced'), are bolded as these are the values used for all geochemical measurements used in Fig. 8. The confidence intervals (CI) are reported as the weighted distribution of the lowest 5% costs to report a 95% confidence interval. The IG-G, ΔIG-G, and ΔIG are the ratio of the interglacial-glacial accumulation ratio, the difference in the IG-G from EDC original (2.09 or 1.85 for only S27 age range), and the change in the proportion of interglacial ice in the record after the applied best fit accumulation and variance scaling factors, respectively. The accumulation rates for EDC are from AICC2023 (Bouchet et al., 2023). The TALDICE IG-G ratio listed here is from Crotti et al., (2022) and the TALDICE δ^2H are from the analysis described in the manuscript and are also limited to the S27 age range.

Code and data availability

Data used in this manuscript that are not already cited will be available on USAP-DC.

Author contributions

A.H. and C.B conceptualized and wrote the original draft; A.H., A.B., E.B., J.M., and Y.Y. assisted with field work; A.H., A.B., C.B., E.B., L.D., A.J.S., E.J.S., N.B., J.I.C., E.O., M.M., E.S. designed analytical methods; A.H., A.B., C.B., E.B., M.K., L.D., A.J.S., E.J.S., N.B., L.K., J.M.M., J.I.C., E.O., M.M., E.S., V.H., J.H assisted with collecting data; A.H., A.B., C.B., and E.B. prepared the manuscript; and A.H., A.B., C.B., E.B., M.K., L.D., A.J.S., E.J.S., N.B., L.K., J.M.M., J.I.C., E.O., Y.Y., V.H., J.H contributed to improving the final paper.

Competing interests

The author Christo Buizert is a member of the editorial board for Climate of the Past.

Disclaimer

Acknowledgements

This work was supported by the U.S. National Science Foundation Center for Oldest Ice Exploration (NSF COLDEX), an NSF Science and Technology Center (NSF-2019719). We thank the NSF Office of Polar Programs, the NSF Office of Integrative Activities, and Oregon State University for financial and infrastructure support, and the NSF Antarctic Infrastructure and Logistics Program, and the Antarctic Support Contractor for logistical support. COLDEX integrates activities in ice coring and analysis, Antarctic exploration and ice sheet modeling, education, knowledge transfer, and broadening participation. All Center components and participants are essential to its success, and contribute to the shared infrastructure that underpins all COLDEX products, including this publication.

Drilling operations were supported by the NSF Ice Drilling Program (NSF-2318480) and the field operations were supported by the U.S. Antarctic Program (USAP) and Kenn Borek Airlines. We are grateful for Elizabeth Morton, Tanner Kuhl, Mike Jayred, and Andrew Haala for their exceptional efforts in drilling and recovering these cores. We also thank Jonathan Hayden, Ema Mayo, Ash Goverman, and Kelcie Meyer for their incredible support in the field for obtaining these cores. We thank the multitude of personnel in USAP and Kenn Borek Airlines who ensured the safe transport of the ice cores from the field to our laboratories. Ice core storage and curation were provided by the NSF Ice Core Facility (NSF-2041950), and we especially thank Richard Nunn, Curt LaBombard, and Theo Carr for their assistance.

Thank you to Eva Lesher who was so helpful in helping cut ice and measure discrete methane for this study. A special thanks to Jenna Epifanio for help with data management, sample allocation, and creation of maps used in this manuscript. We are grateful to the COLDEX team members for building a collaborative community that promoted new ideas and provided valuable feedback throughout this work. Thank you to Ali Jones who crafted an incredible software for the OSU CFA lab.

Financial support

U.S. National Science Foundation Center for Oldest Ice Exploration (NSF COLDEX), an NSF Science and Technology Center (NSF-2019719), NSF Ice Drilling Program (NSF-2318480), and NSF Ice Core Facility (NSF-2041950).

Review statement

The review statement will be added by Copernicus Publications listing the handling editor as well as all contributing referees according to their status anonymous or identified.

References

Baccolo, G., Delmonte, B., Di Stefano, E., Cibin, G., Crotti, I., Frezzotti, M., Hampai, D., Iizuka, Y., Marcelli, A., & Maggi, V. (2021). Deep ice as a geochemical reactor: Insights from iron speciation and mineralogy of dust in the Talos Dome ice core (East Antarctica). *Cryosphere*, *15*(10), 4807–4822. https://doi.org/10.5194/tc-15-4807-2021

Baccolo, G., Delmonte, B., Niles, P. B., Cibin, G., Di Stefano, E., Hampai, D., Keller, L., Maggi, V., Marcelli, A., Michalski, J., Snead, C., & Frezzotti, M. (2021). Jarosite formation in deep Antarctic ice provides a window into acidic, water-limited weathering on Mars. *Nature Communications*, *12*(1). https://doi.org/10.1038/s41467-020-20705-z

Baggenstos, D., Severinghaus, J. P., Mulvaney, R., McConnell, J. R., Sigl, M., Maselli, O., Petit, J. R., Grente, B., & Steig, E. J. (2018). A Horizontal Ice Core From Taylor Glacier, Its Implications for Antarctic Climate History, and an Improved Taylor Dome Ice Core Time Scale. *Paleoceanography and Paleoclimatology*, *33*(7), 778–794. https://doi.org/10.1029/2017PA003297

Bender, M. L., Barnett, B., Dreyfus, G., Jouzel, J., & Porcelli, D. (2008). The contemporary degassing rate of 40Ar from the solid Earth. *Proceedings of the National Academy of Sciences of the United States of America*, *105*(24), 8232–8237. https://doi.org/10.1073/pnas.0711679105

Berends, C. J., Köhler, P., Lourens, L. J., & van de Wal, R. S. W. (2021). On the Cause of the Mid-Pleistocene Transition. In *Reviews of Geophysics* (Vol. 59, Number 2). John Wiley and Sons Inc. https://doi.org/10.1029/2020RG000727

Bintanja, R. (1999). On the glaciological, meteorological, and climatological significance of Antarctic blue ice areas. *Reviews of Geophysics*, *37*(3), 337–359. https://doi.org/10.1029/1999RG900007

Bouchet, M., Landais, A., Grisart, A., Parrenin, F., Prié, F., Jacob, R., Fourré, E., Capron, E., Raynaud, D., Lipenkov, V. Y., Loutre, M. F., Extier, T., Svensson, A., Legrain, E., Martinerie, P., Leuenberger, M., Jiang, W., Ritterbusch, F., Lu, Z. T., & Yang, G. M. (2023). The Antarctic Ice Core Chronology 2023 (AICC2023) chronological framework and associated timescale for the European Project for Ice Coring in Antarctica (EPICA) Dome C ice core. *Climate of the Past*, *19*(11), 2257–2286. https://doi.org/10.5194/cp-19-2257-2023

Burton, L. E., Oldeman, A. M., Haywood, A. M., Tindall, J. C., Dolan, A. M., Hill, D. J., von der Heydt, A., & Baatsen, M. L. J. (2025). An assessment of the Pliocene as an analogue for our warmer future. *Global and Planetary Change*, *252*. https://doi.org/10.1016/j.gloplacha.2025.104860

Carter, A. J., Aarons, S. M., Schnaubelt, J. C., Tabor, C. R., Shackleton, S. A., Epifanio, J. A., Morgan, J. D., Davies, G. R., Gabrielli, P., Choi, A., Severinghaus, J. P., Brook, E. J., Introne, D. S., Marks Peterson, J. C., Sutter, J., & Davidge, L. (In press). *Evidence for a diminished Ross Ice Shelf and West Antarctic Ice Sheet during MIS 5e*.

Chesler, A., Winski, D., Kreutz, K., Koffman, B., Osterberg, E., Ferris, D., Thundercloud, Z., Mohan, J., Cole-Dai, J., Wells, M., Handley, M., Anderson, K., & Harmon, N. (2022). *Non-spherical microparticle shape in Antarctica during the last glacial period affects dust volume-related metrics*. (May). https://doi.org/10.5194/cp-2022-36

Clark, P. U., Archer, D., Pollard, D., Blum, J. D., Rial, J. A., Brovkin, V., Mix, A. C., Pisias, N. G., & Roy, M. (2006). The middle Pleistocene transition: characteristics, mechanisms, and implications for long-term changes in atmospheric pCO2. *Quaternary Science Reviews*, *25*(23–24), 3150–3184. https://doi.org/10.1016/j.quascirev.2006.07.008

Crotti, I., Quiquet, A., Landais, A., Stenni, B., Wilson, D. J., Severi, M., Mulvaney, R., Wilhelms, F., Barbante, C., & Frezzotti, M. (2022). Wilkes subglacial basin ice sheet response to Southern Ocean warming during late Pleistocene interglacials. *Nature Communications*, *13*(1). https://doi.org/10.1038/s41467-022-32847-3

Davidge, L., Steig, E. J., & Schauer, A. J. (2022). Improving continuous-flow analysis of triple oxygen isotopes in ice cores: insights from replicate measurements. *Atmospheric Measurement Techniques*, *15*(24), 7337–7351. https://doi.org/10.5194/amt-15-7337-2022

EPICA community members. (2004). Eight glacial cycles from an Antarctic ice core. *Nature*, *429*, 623–628. https://doi.org/10.1038/nature02599

Epifanio, J. A., Brook, E. J., Buizert, C., Edwards, J. S., Sowers, T. A., Kahle, E. C., Severinghaus, J. P., Steig, E. J., Winski, D. A., Osterberg, E. C., Fudge, T. J., Aydin, M., Hood, E., Kalk, M., Kreutz, K. J., Ferris, D. G., & Kennedy, J. A. (2020). The SP19 chronology for the South Pole Ice Core - Part 2: Gas chronology, Δage, and smoothing of atmospheric records. *Climate of the Past*, *16*(6), 2431–2444. https://doi.org/10.5194/cp-16-2431-2020

Fitzpatrick, J. J., Voigt, D. E., Fegyveresi, J. M., Stevens, N. T., Spencer, M. K., Cole-Dai, J., Alley, R. B., Jardine, G. E., Cravens, E. D., Wilen, L. A., Fudge, T. J., & McConnell, J. R. (2014). Physical properties of the WAIS divide ice core. In *Journal of Glaciology* (Vol. 60, Number 224, pp. 1140–1154). International Glaciology Society. https://doi.org/10.3189/2014JoG14J100

Ford, B. H. L., & Chalk, T. B. (2020). The Mid-Pleistocene Enigma. *Oceanography*, *33*(2), 101–103.

Gkinis, V., Popp, T. J., Blunier, T., Bigler, M., Schüpbach, S., Kettner, E., & Johnsen, S. J. (2011). Water isotopic ratios from a continuously melted ice core sample. *Atmospheric Measurement Techniques*, *4*(11), 2531–2542. https://doi.org/10.5194/amt-4-2531-2011

Grinsted, A., Moore, J., Spikes, V. B., & Sinisalo, A. (2003). Dating Antarctic blue ice areas using a novel ice flow model. *Geophysical Research Letters*, *30*(19). https://doi.org/10.1029/2003GL017957

Haywood, A. M., Tindall, J. C., Dowsett, H. J., Dolan, A. M., Foley, K. M., Hunter, S. J., Hill, D. J., Chan, W. Le, Abe-Ouchi, A., Stepanek, C., Lohmann, G., Chandan, D., Richard Peltier, W., Tan, N., Contoux, C., Ramstein, G., Li, X., Zhang, Z., Guo, C., … Lunt, D. J. (2020). The Pliocene Model Intercomparison Project Phase 2: Large-scale climate features and climate sensitivity. *Climate of the Past*, *16*(6), 2095–2123. https://doi.org/10.5194/cp-16-2095-2020

Higgins, J. A., Kurbatov, A. V., Spaulding, N. E., Brook, E., Introne, D. S., Chimiak, L. M., Yan, Y., Mayewski, P. A., & Bender, M. L. (2015). Atmospheric composition 1 million years ago from blue ice in the Allan Hills, Antarctica. *Proceedings of the National Academy of Sciences of the United States of America*, *112*(22), 6887–6891. https://doi.org/10.1073/pnas.1420232112

Higgins, J. H. V. K. L. S. Eric. J. (2026). *40Ar-atm and δ18O data for Allan Hills ice cores ALHIC 2301, ALHIC 2302, ALHIC 2201*.

Hu, J., Yan, Y., Yeung, L. Y., & Dee, S. G. (2022). Sublimation Origin of Negative Deuterium Excess Observed in Snow and Ice Samples From McMurdo Dry Valleys and Allan Hills Blue Ice Areas, East Antarctica. *Journal of Geophysical Research: Atmospheres*, *127*(11). https://doi.org/10.1029/2021JD035950

Jones, T. R., White, J. W. C., Steig, E. J., Vaughn, B. H., Morris, V., Gkinis, V., Markle, B. R., & Schoenemann, S. W. (2017a). Improved methodologies for continuous-flow analysis of stable water isotopes in ice cores. *Atmospheric Measurement Techniques*, *10*(2), 617–632. https://doi.org/10.5194/amt-10-617-2017

Jones, T. R., White, J. W. C., Steig, E. J., Vaughn, B. H., Morris, V., Gkinis, V., Markle, B. R., & Schoenemann, S. W. (2017b). Improved methodologies for continuous-flow analysis of stable water isotopes in ice cores. *Atmospheric Measurement Techniques*, *10*(2), 617–632. https://doi.org/10.5194/amt-10-617-2017

Kirkpatrick, L., Carter, A., Marks-Peterson, J., Shackleton, S., & Fudge, T. J. (2025). Three-Dimensional Multitrack Electrical Conductivity Method for Interpretation of Complex Ice Core Stratigraphy. *Journal of Glaciology*. https://doi.org/10.1017/jog.2025.10081

Kuhl, T. W., Johnson, J. A., Shturmakov, A. J., Goetz, J. J., Gibson, C. J., & Lebar, D. A. (2014). A new large-diameter ice-core drill: The Blue Ice Drill. *Annals of Glaciology*, *55*(68), 1–6. https://doi.org/10.3189/2014AoG68A009

Lambert, F., Bigler, M., Steffensen, J. P., Hutterli, M., & Fischer, H. (2012). Centennial mineral dust variability in high-resolution ice core data from Dome C, Antarctica. *Climate of the Past*, *8*(2), 609–623. https://doi.org/10.5194/cp-8-609-2012

Landais, A., Stenni, B., Masson-Delmotte, V., Jouzel, J., Cauquoin, A., Fourré, E., Minster, B., Selmo, E., Extier, T., Werner, M., Vimeux, F., Uemura, R., Crotti, I., & Grisart, A. (2021). Interglacial Antarctic–Southern Ocean climate decoupling due to moisture source area shifts. *Nature Geoscience*, *14*(12), 918–923. https://doi.org/10.1038/s41561-021-00856-4

Lee, J. E., Edwards, J. S., Schmitt, J., Fischer, H., Bock, M., & Brook, E. J. (2020). Excess methane in Greenland ice cores associated with high dust concentrations. *Geochimica et Cosmochimica Acta*, *270*, 409–430. https://doi.org/10.1016/j.gca.2019.11.020

Marks-Peterson, J., Shackleton, S., Higgins, J., Severinghaus, J., Yan, Y., Buizert, C., Kalk, M., Beaudette, R., Hishamunda, V., Eves, D., Carter, A., Kurbatov, A., Epifanio, J., Morgan, J., Nesbitt, I., Bender, M., & Brook, E. (2026). Broadly stable atmospheric CO2 and CH4 levels over the past 3 million years. *Nature*, *651*(8106), 647–652. https://doi.org/10.1038/s41586-025-10032-y

Masson-Delmotte, V., Hou, S., Ekaykin, A., Jouzel, J., Aristarain, A., Bernardo, R. T., Bromwich, D., Cattani, O., Delmotte, M. M., Falourd, S., Frezzotti, M., Gallée, H., Genoni, L., Isaksson, E., Landais, A., Helsen, M. M., Hoffmann, G., Lopez, J., Morgan, V., … White, J. W. C. (2008). A review of antarctic surface snow isotopic composition: Observations, atmospheric circulation, and isotopic modeling. In *Journal of Climate* (Vol. 21, Number 13, pp. 3359–3387). https://doi.org/10.1175/2007JCLI2139.1

Mühl, M., Schmitt, J., Seth, B., Lee, J. E., Edwards, J. S., Brook, E. J., Blunier, T., & Fischer, H. (2023). Methane, ethane, and propane production in Greenland ice core samples and a first isotopic characterization of excess methane. *Climate of the Past*, *19*(5), 999–1025. https://doi.org/10.5194/cp-19-999-2023

Nesbitt, I. M. ; B. Edward. J. (2023). *I-165-M GPR Field Report 2019-2020* .

Osterberg, E. C., Handley, M. J., Sneed, S. B., Mayewski, P. A., & Kreutz, K. J. (2006). Continuous ice core melter system with discrete sampling for major ion, trace element, and stable isotope analyses. *Environmental Science and Technology*, *40*(10), 3355–3361. https://doi.org/10.1021/es052536w

Paul Voosen. (2021). Hunt begins for ancient Antarctic ice. *Science*, *374*(6566), 388–389.

Rhodes, R. H., Brook, E. J., Chiang, J. C. H., Blunier, T., Maselli, O. J., McConnell, J. R., Romanini, D., & Severinghaus, J. P. (2015). Enhanced tropical methane production in response to iceberg discharge in the North Atlantic. *Science*, *348*(6238), 1016–1019. https://doi.org/10.1126/science.1262005

Rhodes, R. H., Faïn, X., Stowasser, C., Blunier, T., Chappellaz, J., McConnell, J. R., Romanini, D., Mitchell, L. E., & Brook, E. J. (2013). Continuous methane measurements from a late Holocene Greenland ice core: Atmospheric and in-situ signals. *Earth and Planetary Science Letters*, *368*, 9–19. https://doi.org/10.1016/j.epsl.2013.02.034

Scarchilli, C., Frezzotti, M., & Ruti, P. M. (2011). Snow precipitation at four ice core sites in East Antarctica: Provenance, seasonality and blocking factors. *Climate Dynamics*, *37*(9–10), 2107–2125. https://doi.org/10.1007/s00382-010-0946-4

Schauer, A. J., Schoenemann, S. W., & Steig, E. J. (2016). Routine high-precision analysis of triple water-isotope ratios using cavity ring-down spectroscopy. *Rapid Communications in Mass Spectrometry*, 2059–2069. https://doi.org/10.1002/rcm.7682

Scherer, P., Schultz, L., Neupert, U., Knauer, M., Neumann, S., Leya, I., Michel, R., Mokos, J., Lipschutz, M. E., Metzler, K., Suter, M., & Kubik, P. W. (1997). Allan Hills 88019: An Antarctic H-chondrite with a very long terrestrial age. *Meteoritics and Planetary Science*, *32*(6), 769–773. https://doi.org/10.1111/j.1945-5100.1997.tb01567.x

Schoenemann, S. W., Schauer, A. J., & Steig, E. J. (2013). Measurement of SLAP2 and GISP δ17O and proposed VSMOW-SLAP normalization for δ17O and 17Oexcess. *Rapid Communications in Mass Spectrometry*, *27*(5), 582–590. https://doi.org/10.1002/rcm.6486

Severinghaus, J., Wolff, E. W., & Brook, E. J. (2010). Searching for the oldest ice. *EOS*, *91*(40), 357–368.

Shackleton, S., Hishamunda, V., Davidge, L., Brook, E., Peterson, J. M., Carter, A., Aarons, S., Kurbatov, A., Introne, D., Yan, Y., Nesbitt, I. M., Buizert, C., Steig, E. J., Schauer, A. J., Morgan, J., Neff, P. D., Epifanio, J. A., Severinghaus, J.,

https://doi.org/10.5194/egusphere-2026-2045
Preprint. Discussion started: 21 April 2026

Bender, M., & Higgins, J. A. (2025). Miocene and Pliocene ice and air from the Allan Hills blue ice area, East Antarctica. *Proceedings of the National Academy of Sciences*, *122*(44). https://doi.org/10.1073/pnas.2502681122

Shackleton, S., Hishamunda, V., Yan, Y., Carter, A., Morgan, J., Severinghaus, J., Aarons, S., Marks-Peterson, J., Epifanio, J., Buizert, C., Brook, E., Kurbatov, A. V., Bender, M. L., & Higgins, J. (2026). Global ocean heat content over the past 3 million years. *Nature*, *651*(8106), 653–657. https://doi.org/10.1038/s41586-026-10116-3

Simonsen, M. F., Cremonesi, L., Baccolo, G., Bosch, S., Delmonte, B., Erhardt, T., Astrid Kjær, H., Potenza, M., Svensson, A., & Vallelonga, P. (2018). Particle shape accounts for instrumental discrepancy in ice core dust size distributions. *Climate of the Past*, *14*(5), 601–608. https://doi.org/10.5194/cp-14-601-2018

Spaulding, N. E., Higgins, J. A., Kurbatov, A. V., Bender, M. L., Arcone, S. A., Campbell, S., Dunbar, N. W., Chimiak, L. M., Introne, D. S., & Mayewski, P. A. (2013). Climate archives from 90 to 250ka in horizontal and vertical ice cores from the allan hills blue ice area, antarctica. *Quaternary Research (United States)*, *80*(3), 562–574. https://doi.org/10.1016/j.yqres.2013.07.004

Spaulding, N. E., Spikes, V. B., Hamilton, G. S., Mayewski, P. A., Dunbar, N. W., Harvey, R. P., Schutt, J., & Kurbatov, A. V. (2012). Ice motion and mass balance at the Allan Hills blue-ice area, Antarctica, with implications for paleoclimate reconstructions. *Journal of Glaciology*, *58*(208), 399–406. https://doi.org/10.3189/2012JoG11J176

Steig, E. J., Gkinis, V., Schauer, A. J., Schoenemann, S. W., Samek, K., Hoffnagle, J., Dennis, K. J., & Tan, S. M. (2014). Calibrated high-precision 17O-excess measurements using cavity ring-down spectroscopy with laser-current-tuned cavity resonance. *Atmospheric Measurement Techniques*, *7*(8), 2421–2435. https://doi.org/10.5194/amt-7-2421-2014

Steig, E. J., Morse, D. L., Waddington, E. D., Stuiver, M., Grootes, P. M., Mayewski, P. A., Twickler, M. S., & Whitlow, S. I. (2000). Wisconsinan and Holocene Climate History from an Ice Core at Taylor Dome, Western RossEmbayment, Antarctica. In *Source: Geografiska Annaler. Series A* (Vol. 82, Number 2).

Stowasser, C., Buizert, C., Gkinis, V., Chappellaz, J., Schapbach, S., Bigler, M., Fan, X., Sperlich, P., Baumgartner, M., Schilt, A., & Blunier, T. (2012). Continuous measurements of methane mixing ratios from ice cores. *Atmospheric Measurement Techniques*, *5*(5), 999–1013. https://doi.org/10.5194/amt-5-999-2012

Tierney, J. E., King, J., Osman, M. B., Abell, J. T., Burls, N. J., Erfani, E., Cooper, V. T., & Feng, R. (2025). Pliocene Warmth and Patterns of Climate Change Inferred From Paleoclimate Data Assimilation. *AGU Advances*, *6*(1). https://doi.org/10.1029/2024AV001356

Whillans, I. M., & Cassidy, W. A. (1983). Catch a Falling Star: Meteorites and Old Ice. In *New Series* (Vol. 222, Number 4619).

Winski, D. A., Fudge, T. J., Ferris, D. G., Osterberg, E. C., Fegyveresi, J. M., Cole-Dai, J., Thundercloud, Z., Cox, T. S., Kreutz, K. J., Ortman, N., Buizert, C., Epifanio, J., Brook, E. J., Beaudette, R., Severinghaus, J., Sowers, T., Steig, E. J., Kahle, E. C., Jones, T. R., … McConnell, J. R. (2019). The SP19 chronology for the South Pole Ice Core - Part 1: Volcanic matching and annual layer counting. *Climate of the Past*, *15*(5), 1793–1808. https://doi.org/10.5194/cp-15-1793-2019

Yan, Y., Bender, M. L., Brook, E. J., Clifford, H. M., Kemeny, P. C., Kurbatov, A. V., Mackay, S., Mayewski, P. A., Ng, J., Severinghaus, J. P., & Higgins, J. A. (2019). Two-million-year-old snapshots of atmospheric gases from Antarctic ice. *Nature*, *574*(7780), 663–666. https://doi.org/10.1038/s41586-019-1692-3

Yan, Y., Spaulding, N. E., Bender, M. L., Brook, E. J., Higgins, J. A., Kurbatov, A. V., & Mayewski, P. A. (2021). Enhanced moisture delivery into Victoria Land, East Antarctica, during the early Last Interglacial: Implications for West Antarctic Ice Sheet stability. *Climate of the Past*, *17*(5), 1841–1855. https://doi.org/10.5194/cp-17-1841-2021